



# Oxidation performance of TP347H superheater steel after depositing ceria-doped Cr<sub>3</sub>C<sub>2</sub>–25NiCr coatings

Harkulvinder Singh<sup>1</sup> · Sukhpal Singh Chatha<sup>1</sup> · Buta Singh Sidhu<sup>2</sup>

Received: 24 January 2022 / Accepted: 27 June 2022 / Published online: 23 July 2022  
© The Author(s), under exclusive licence to Springer Nature Switzerland AG 2022

## Abstract

Oxidation is the predominant corrosion mode, which consumes the material from the surface. During oxidation, the formation of oxide layer resists the further corrosion attack. However, due to the stresses developed during the growth of the oxide scale, the spallation/delamination takes place, resulting in the exposure of fresh material to the corrosive environment. In the current investigation, ceria blended Cr<sub>3</sub>C<sub>2</sub>–NiCr composite coatings were applied on TP347H austenite steel substrates with a HIPOJET-2700 spraying gun. Three mixture ratios of cerium (0.4 wt-%, 0.8 wt-%, and 1.2 wt-%) were selected for exploring the coating performance under an oxidation environment at 750 °C for 50 cycles. The microstructure and corrosion kinetics of the coating are evaluated using SEM/EDS, XRD, and X-ray mapping analysis. Moreover, the effect of the addition of cerium towards microhardness, surface roughness, and microporosity was compared with conventional Cr<sub>3</sub>C<sub>2</sub>–NiCr coating. The results indicated that the 0.4 wt-% of ceria added Cr<sub>3</sub>C<sub>2</sub>–NiCr coating provides better oxidation resistance than its counterparts, which might be attributed to the growing thin and compact oxide scale of Cr<sub>2</sub>O<sub>3</sub>, Ce<sub>2</sub>O<sub>3</sub>, and NiCr<sub>2</sub>O<sub>4</sub>, CeCrO<sub>3</sub> spinels. As the percentage of ceria increases in the coating, the oxide scale adherence decreases, which might be due to the massive concentration of oxygen that pickup by cerium oxide particles and increases microporosity of the coating or oxide scale; simultaneously, the oxidation resistance of coated substrate decreases.

**Keywords** TP347H steel · Oxidation · Coatings · Rare earth element

## 1 Introduction

Most of the industrial components in heating furnaces, heating ovens, boilers, turbines, internal combustion engines, rollers, chimneys, rotary mills operate at high temperature in the presence of a gaseous environment (Muthu et al. 2020; Nithin et al. 2020). These components are basically made up of iron along with other elements. This basic element comes in contact with the surrounding environment, and the reaction takes place on the surface of metals and alloys, which develop compounds is known as 'corrosion.' When this corrosion is associated with high temperature, then its severity to degradation increases. This process of material deterioration is known as 'oxidation' (Goyal et al. 2012;

Prabhakaran and Jegadeeswaran 2021). Due to oxidation, the protective/non-protective layer formed after nucleation and growth process on the surface of the underlying material, which may or may not protect further reactions (Goyal et al. 2017). Some metals/alloys develop a protective oxide scale under an N<sub>2</sub> gaseous environment, whereas scale failure occurs under CO and CO<sub>2</sub> due to embrittlement (Saroop et al. 2020). The power plant, petrochemical, textile, cement, fertilizer, marine, waste incinerators, automobiles, nuclear reactors, and aerospace industries mainly suffer from surface degradation due to 'oxidation' phenomena (Chawla et al. 2011; Ghosh and Mitra 2011). The working strength of the material is greatly influenced by oxidation, sulfidation, and hot corrosion reactions at high temperature. This limits the life span of the industrial components that work in an aggressive environment. Three factors can measure the rate of oxidation; the first one is the oxygen consumption by metal or alloy during service, the second one is the amount of metal consumption during a chemical reaction, and the last one is the amount of oxides produced on the surface of metal/alloy (Khanna 2016; Saroop et al. 2020). From

✉ Harkulvinder Singh  
harkulvinder2018@gmail.com

<sup>1</sup> Yadavindra Department of Engineering, Punjabi University  
Guru Kashi Campus, Talwandi Sabo, Punjab 151302, India

<sup>2</sup> Maharaja Ranjit Singh Punjab Technical University,  
Bathinda, Punjab 151001, India

the above, the weight change measurements after metal consumption (weight gain or loss/Thickness gain or loss) is the least preferable method for oxidation kinetics (Perez 2016).

Further, oxidation kinetics is based on three laws, namely, linear law, parabolic law, and logarithm law. The degradation effect of the oxidation reaction is primarily controlled by altering the composition of alloys. The iron-based alloys (steels) have been developed to encounter oxidational degradation. These alloys are categorized based on crystal structure: ferritic steel, martensitic, and austenitic steel. Despite their considerable strength, steel alloys have minor corrosion (oxidation) resistance, and it further demands additional surface treatments such as coatings to shield the surfaces from hostile environments. Surfaces have traditionally been coated to defend them from hazardous chemical and physical interactions with the environment (Guo et al. 2015; Gada et al. 2020). The thermal spraying technology is a cost-effective solution to enhance the surface qualities of structural steels for high-temperature applications in a variety of uses. From the family of thermal spray processes, the most effective method is High-Velocity Oxy-Fuel (HVOF), which combines a low-temperature flame with a high velocity to reduce inflight particle oxidation during spraying. So, the coatings achieved with the HVOF technique are denser, have high adhesive strength, high hardness, and low porosity, which are the desired characteristics of coating (Houdková et al. 2015; Ding et al. 2015; Sreenivasulu and Manikandan 2018). The various types of metallic (Ni–Cr, NiCrAlY, Tribo-alloy, Cr<sub>3</sub>C<sub>2</sub>–NiCr), carbides (TiC, Cr<sub>3</sub>C<sub>2</sub>, SiC, WC, etc.), and oxide (Cr<sub>2</sub>O<sub>3</sub>, Al<sub>2</sub>O<sub>3</sub>, ZrO<sub>2</sub>, TiO<sub>2</sub>) powders are used to combat oxidation, hot corrosion, and wear of the substrate material (Mehta et al. 2017). Due to the superiority of Cr<sub>x</sub>C<sub>y</sub>–NiCr composition at high temperature, it is commercially used for protecting waste incineration plants, electric furnaces, refineries, and power plant components (Ksiazek et al. 2016; Singh et al. 2019; Matthews and Berger 2019; Shi et al. 2020). Carbides in the coatings provide high hardness (750Hv–950Hv), whereas NiCr improves the oxidation and hot corrosion resistance up to 900 °C. Besides the above properties, chromium carbide have similar thermal expansion as of Fe and Ni, so these elements alloyed in every structural component that operates at high-temperature (Shukla et al. 2015; Mathapati et al. 2018).

Ding et al. (2015) examined the oxidation mechanism of HVOF deposited NiCr–Cr<sub>3</sub>C<sub>2</sub> coatings on 304 boiler steels. The results showed that Cr<sub>2</sub>O<sub>3</sub> oxides protect the underlying material from oxidation at 700 °C and 800 °C. The angular grain size changes from fine to enlarge during oxidation study. (Da Cunha et al. 2017) examined the oxidation and erosion resistance of chromium carbide coatings on AISI-310 steels using the HVOF process. The investigation was done at 450 °C, 700 °C, and 800 °C for 5 h in the laboratory environment. Carbide coating is mainly damaged by

erosion oxidation at 450 °C, but at a higher temperature range, the coating protects due to the oxide layer developed on the surface of the coating. (Houdková et al. 2018) investigated the wear and oxidation of modified carbide-based coatings (Cr<sub>3</sub>C<sub>2</sub>–NiCr; Cr<sub>3</sub>C<sub>2</sub>–CoNiCrAlY, and Cr<sub>3</sub>C<sub>2</sub>–NiCr–MoNb) formulated using the HIPOJET gun on carbon steel. The results showed that MoNb doped carbide coating performed better in oxidation, whereas Cr<sub>3</sub>C<sub>2</sub>–NiCr + CoAlY coating enhanced wear resistance at 600 °C. (Kumar et al. 2018, 2019a) evaluated oxidation performance of WC–CO and Cr<sub>3</sub>C<sub>2</sub>–NiCr coatings after deposition with D-gun spraying on T-91 and SA-216 substrate material. The results revealed that chromium carbide coating remained intact to the substrate and maintained adherence at 800 °C, but WC–CO coating was delaminated from the sample surface during the cyclic study. The features of carbide coatings are reduced up to some extent after stress generation from thermal mismatch during cyclic fluctuations (Panicaud et al. 2006). The coating's stability and endurance are determined by the microstructure's homogeneity and the protective oxide scale's adherence to the surface (Zhou et al. 2016; Ghadami et al. 2021). Cracking and spallation of coating may occur due to stress generating in the coating at high temperature (Yedong and Wei 2013). So, some modifications are made in the composition of feedstock powder, which improves the microstructure of the coatings. The oxidation and hot corrosion behaviour of alloys and coatings after blending reactive elements (RE) has been studied by various researchers. Authors have reported the beneficial effect of incorporation of RE elements (Lanthanides) in the coatings, i.e., refinement of microstructure, pegging of grain boundaries, reduction in oxide growth stress, and adherence of coating/substrate interface (Thanneeru et al. 2007; Nijdam and Sloof 2007; Kumar et al. 2014; Zhang et al. 2014). The mechanisms proposed by various researchers regarding improvement in oxidation resistance are primarily due to the migration of rare earth element ions to the oxide grain boundaries and retard the movement of alloy cation diffusion from the metal/oxide towards the oxide/air interface (Pilllis et al. 2006). There is a total of 17 lanthanide series of rare earth elements. From the existing series, cerium oxide (CeO<sub>2</sub>) is the most important element because of its rich oxygen vacancy defects and higher capacity to release or absorb oxygen molecules that plays an essential role in generating a protective oxide layer (Wang et al. 2020). Some studies examined that the doping of Ce lanthanide in the coating can decrease the growth rate of oxides and porosity at scale/substrate interface (You et al. 2018). (Zhu et al. 2004) studied the oxidation performance of Ni + CeO<sub>2</sub> coatings deposited on mild carbon substrate under a dry air environment at 840 °C for 120 h. The results showed that Ni + CeO<sub>2</sub> composite coating enhances the oxidation resistance due to the slow growth of oxides, and fine grain structure gives more

adhesion to coating. (Huiming et al. 2007) examined the oxidation behaviour of  $\text{CeO}_2$ -coated chromium substrate in the laboratory. The analyzed results showed that  $\text{CeO}_2$  coatings significantly reduced the growth rate and grain size of  $\text{Cr}_2\text{O}_3$  and enhanced the oxide scale plasticity. Kamal et al. (2011), Chen et al. (2014), Mahesh et al. (2010), and Liu et al. (2020b) describe that the addition of cerium oxide in NiCrAlY feedstock provides better oxidation resistance attributed to the generation of adherent oxide scale. Mudgal et al. (2014, 2015), Kumar et al. (2014), Saladi et al. (2015), and Ahuja and Mudgal (2019) reported that the addition of  $\text{CeO}_2$  element has increased adherence and oxidation resistance of the d-gun sprayed  $\text{Cr}_3\text{C}_2$ -NiCr coatings at 900 °C in waste incinerator environments. (Wang and Szpunar 2017) examined the oxidation resistance of  $\text{CeO}_2$ -coated Ni-based alloy (230) in dry air at 900 °C for 1000 h.  $\text{CeO}_2$  particle changes the diffusion mechanism of oxygen from outward to inward, which converts columnar grains structure of  $\text{Cr}_2\text{O}_3$  to equiaxed structure that enhances the spallation resistance of oxide layer.

Several studies in the literature have stated the effect of rare earth element doping in the alloy. Nevertheless, only limited investigations have been reported related to the oxidation performance of rare earth elements containing coatings.

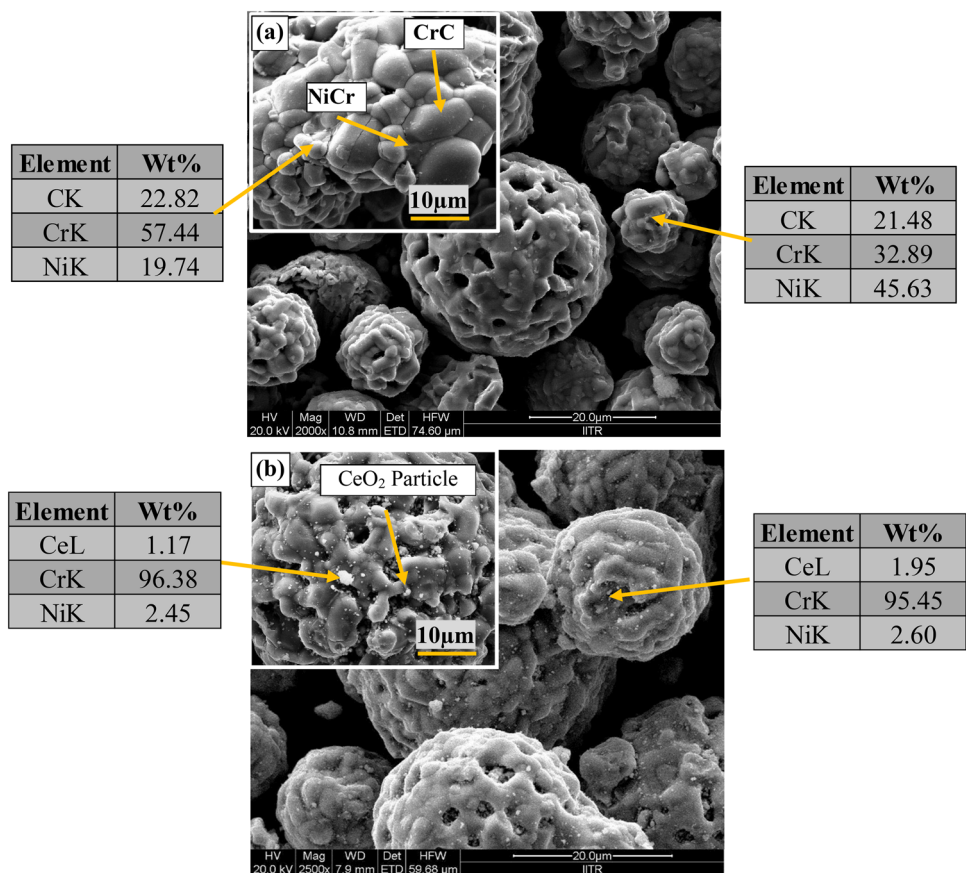
Nevertheless, most earlier researches on the oxidation performance of  $\text{Cr}_3\text{C}_2$ -NiCr-coated ferritic steels, superalloys, and austenite steels have been conducted at temperatures below 900 °C. Furthermore, the effect of different alloying elements and rare earth elements with different ratios (wt.%) on the oxidation study of austenite steel at higher temperatures is unknown. Thus, it is intriguing to examine the effect of RE elements in different ratio in conventional carbide ( $\text{Cr}_3\text{C}_2$ -NiCr) coating to improve austenite stainless steels' oxidation behaviour. There is no reported literature at present for optimum quantity (wt.%) of RE added  $\text{Cr}_3\text{C}_2$ -25NiCr coatings deposited using HVOF on TP347H austenite steel exposed to 750 °C for cyclic oxidation. Moreover, the influence of  $\text{CeO}_2$  on the oxide scale is investigated in the present study.

## 2 Experimental

### 2.1 Materials and coating formulation

The gas atomized 75 $\text{Cr}_3\text{C}_2$ -25(Ni-20Cr) powder obtained from H.C. STARCK, AMPERIT® Germany, was utilized as the feedstock for coating the samples. Moreover, cerium

**Fig. 1** FESEM micrograph of coating powders; a  $\text{Cr}_3\text{C}_2$ -NiCr; b  $\text{CeO}_2$ -doped  $\text{Cr}_3\text{C}_2$ -NiCr with EDS analysis



**Table 1** Characteristics of feedstock

Characteristics	Cr <sub>3</sub> C <sub>2</sub> -25NiCr	Cerium oxide (CeO <sub>2</sub> )
Product code	584.054	211,575
Particle size	– 45 + 5 (μm)	< 5 (μm)
Powder morphology	Spheroidal	Cylindrical
Powder Colour	Dark grey	White to yellow
Manufacturing process	Gas atomized	–
Company	H.C. Starck, Germany	Sigma Aldrich, USA

oxide (Sigma Aldrich, USA) with purity of 99.99% (Product Code: 544,841) was blended with Cr<sub>3</sub>C<sub>2</sub>-25NiCr feedstock, to produce three different compositions (0.4 wt-% CeO<sub>2</sub> + Cr<sub>3</sub>C<sub>2</sub>-25NiCr, 0.8 wt-% CeO<sub>2</sub> + Cr<sub>3</sub>C<sub>2</sub>-25NiCr, and 1.2 wt-% CeO<sub>2</sub> + Cr<sub>3</sub>C<sub>2</sub>-25NiCr). The mixing of the powders was done using conventional jar milling for 6 h. Figure 1a, b show the powder morphology for conventional Cr<sub>3</sub>C<sub>2</sub>-25NiCr, and ceria-doped Cr<sub>3</sub>C<sub>2</sub>-25NiCr powder with EDS analysis. In the present investigation, the substrate was selected as austenite (TP347H) steel having dimensions 20 mm × 15 mm × 5 mm. The main characteristics of feedstock and substrate material are given in Tables 1 and 2, respectively. The abbreviations used for each coating are given in Table 3. Before the spraying, the surface of substrates was cleaned with different grades of emery papers and then grit blasted using alumina to get a uniform and clean surface finish. High-Velocity Oxy-Fuel (HIPOJET-2700) thermal spraying gun provided by MECPL Rajasthan, India, was utilized to formulate coatings on substrate steel. Around 220–280 μm thick coating was formulated on austenite steel substrates. The HVOF spraying constraints employed for the coatings are given in Table 4.

## 2.2 Characterization of feedstock and coatings

The microstructure of the powders and HVOF deposited coatings, as well as morphology from surface and cross-section, were examined by field emission scanning electron microscopy (JEOL-7610Plus, Japan), energy dispersive spectroscopy (EDS, EDAX/APEX), and X-ray mapping. Bruker diffractometer (D8 ADVANCE, Germany) with Cu-Kα radiation was used for chemical analysis. Xpert High

**Table 2** Actual composition (wt.%) of TP347H steel

Element	Cr	Ni	C	Mn	P	S	Si	Nb	Fe
Wt%	17.53	11.42	0.067	1.54	0.024	0.001	0.59	0.70	Bal

**Table 3** Abbreviations used for each coating during present study

Coating composition	Designation
1. Cr <sub>3</sub> C <sub>2</sub> -25NiCr	OH
2. Cr <sub>3</sub> C <sub>2</sub> -25NiCr + Ce (0.4wt-%)	OH1
3. Cr <sub>3</sub> C <sub>2</sub> -25NiCr + Ce (0.8wt-%)	OH3
4. Cr <sub>3</sub> C <sub>2</sub> -25NiCr + Ce (1.2wt-%)	OH5

Score Plus software was used to calculate the d-spacing value provided by the diffractometer. The surface roughness of the as-sprayed coatings was calculated using a stylus type (Tip radius 2 μm) surface roughness tester (Mitutoyo SJ-201, Japan) with a measuring force of 0.75mN with a speed of 0.01 Inch/S. The sampling length is taken as 0.8 mm (No. of sampling lengths-5), and cut off the length was (0.05 mm). An average surface roughness was calculated from five readings per specimen. For the x-sectional study, HVOF-coated substrates were cut using Metallurgical Sample Saw MS-10 (DUCOM) at a slow speed and fixed in epoxy with Bainmount H-Auto (METCO) machine. Further, standard polishing was done with emery papers followed by cloth polishing. The microporosity was measured using Image-J (1.8.0) software, and the microhardness of the coatings was observed using Mitutoyo hardness tester (HM-211, Japan) with a test load of 1KN. The test load of 0.5KN was applied for a total of 10 s, including loading, dwell, and unloading. An average of at least five indents was taken from measurements in regions of dense coating material. An average hardness was calculated from five indents per specimen.

## 2.3 Oxidation studies

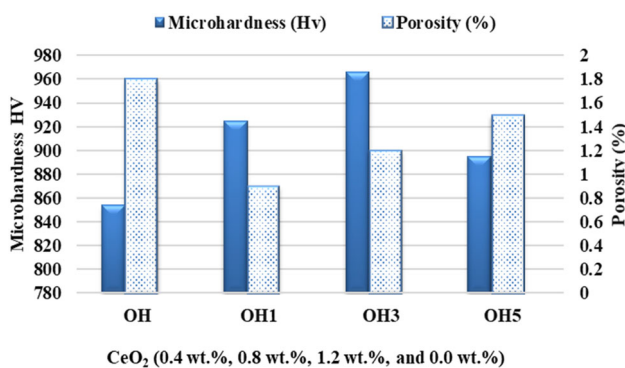
The high-temperature oxidation testing was carried out in a silicon carbide furnace at 750 °C for 50 cycles. The temperature of the tube furnace is controlled with a PID controller attached with a K-type thermocouple. The surface area of the samples was calculated with a Vernier caliper. The samples were washed with acetone to remove the impurities from the surface. Alumina boats were cured at 1000 °C for 10 h and cooled in ambient air. Afterward, the samples were pre-heated in an oven along with the alumina boat for 1 h at 150 °C. The weight was measured after oven heating with an electronic weighing machine (CITIZEN, CB-120), having an accuracy of 0.01 mg. Then, the alumina boat with the sample was kept in the SiC tube furnace at 750 °C for



**Table 4** Spray Parameters employed for HVOF coating (HIPOJET 2700)

Parameter	Value
Oxygen flow rate	200 SLPM
Fuel (LPG) flow rate	50 SLPM
Air-flow rate	900 SLPM
Spray distance	200 mm
Powder feed rate	38 to 40 gm/min
Fuel pressure	6.00 kg/cm <sup>2</sup>
Oxygen pressure	8.00 kg/cm <sup>2</sup>
Air pressure	6.00 kg/cm <sup>2</sup>
Flame temperature	1900–2200 °C

SLPM stands for litre per minute\*

**Fig. 2** Microhardness and porosity measurements for conventional and modified Cr<sub>3</sub>C<sub>2</sub>–NiCr coatings with different contents of CeO<sub>2</sub>

1 h. After each cycle, the change in colour variation, lustre (dull/bright), scale spallation (cracks/delamination) was also visually assessed for each sample. The kinematics of air oxidation were determined using the weight change value. The oxidized samples were characterized from the surface and cross-section using SEM/EDS, XRD, and X-ray map techniques after being exposed for 50 cycles.

## 3 Results

### 3.1 Coating characterization

The microhardness and microporosity of the HVOF as-sprayed coatings were analysed, and the observations are presented in Fig. 2. The porosity of the Cr<sub>3</sub>C<sub>2</sub>–NiCr coating (OH) is observed to be 1.8%. Further, it is observed that the addition of ceria into Cr<sub>3</sub>C<sub>2</sub>–NiCr coating resulted in a decrease in porosity, and the lowest porosity is observed for Cr<sub>3</sub>C<sub>2</sub>–NiCr coating modified with 0.4wt-% of CeO<sub>2</sub>. However, further increase in wt-%age of ceria resulted in increase

in porosity for Cr<sub>3</sub>C<sub>2</sub>–NiCr + 0.8 wt-% CeO<sub>2</sub> (OH3) and Cr<sub>3</sub>C<sub>2</sub>–NiCr + 1.2 wt-% CeO<sub>2</sub> (OH5) coatings. The decrease in porosity with the addition of CeO<sub>2</sub> may be attributed to grain refinement of the coatings (Purkayastha and Dwivedi 2014; Ghadami et al. 2019).

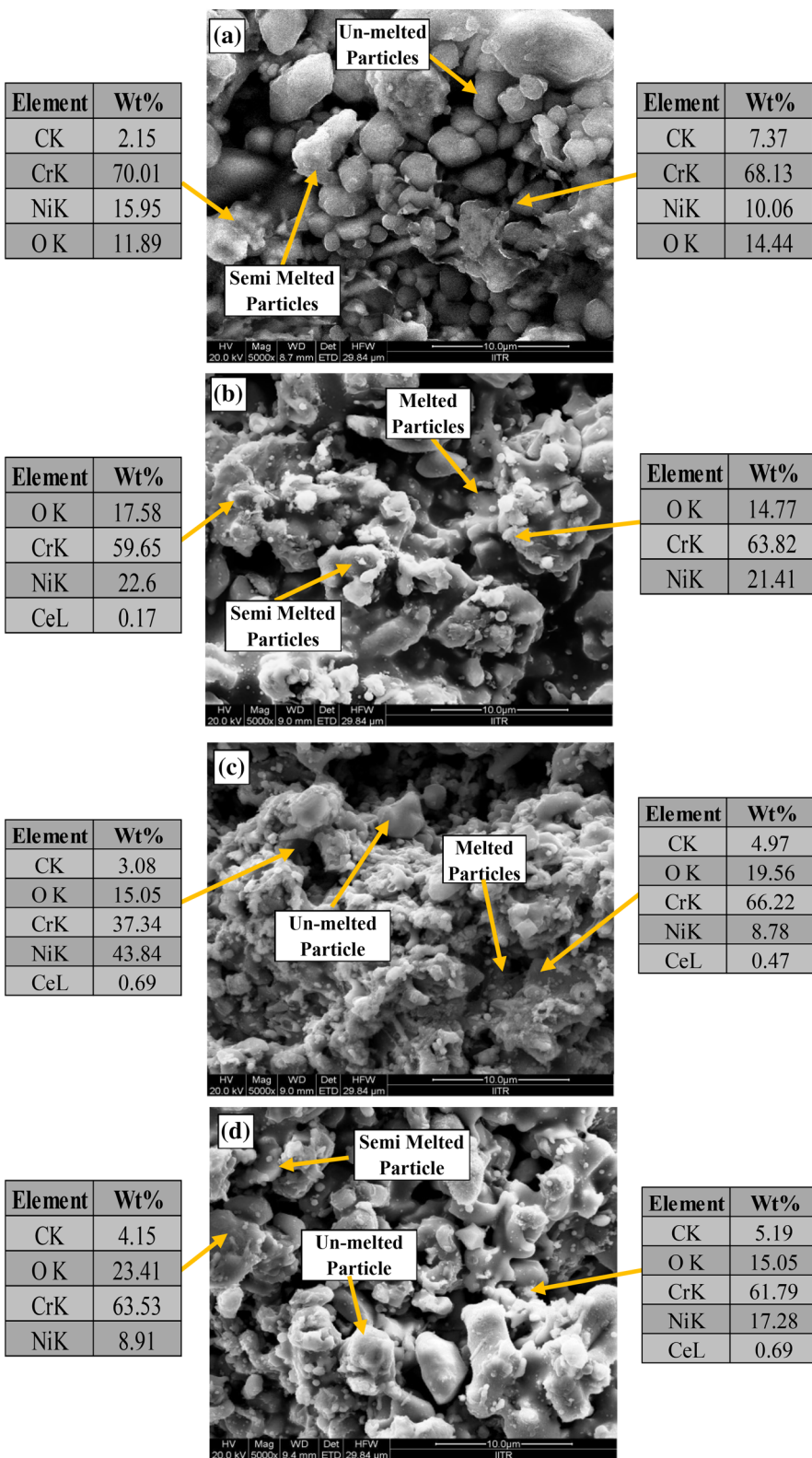
Figure 2 indicated that OH coating possesses an average microhardness of 854Hv. Further, it is observed that the doping of CeO<sub>2</sub> enhances the microhardness of conventional (OH) Cr<sub>3</sub>C<sub>2</sub>–NiCr coating, which may be due to the refinement of grains with heterogeneous nucleation mechanisms (Sharma 2012). OH3, coating doped with 0.8wt-% of CeO<sub>2</sub> exhibited maximum value (966Hv) of microhardness, followed by OH1 coating (925Hv) doped with 0.4wt-% and OH5 coating (895Hv) doped with 1.2 wt-% of CeO<sub>2</sub>. It is well known that RE elements can refine the microstructure of coatings due to their ability to release and store oxygen during oxidation. Moreover, it acts as a nucleation site during the solidification of coating, resulting in heterogeneous nucleation, which hinders the growth of gains throughout the crystallization (Cai and Li 2015; Shu et al. 2020).

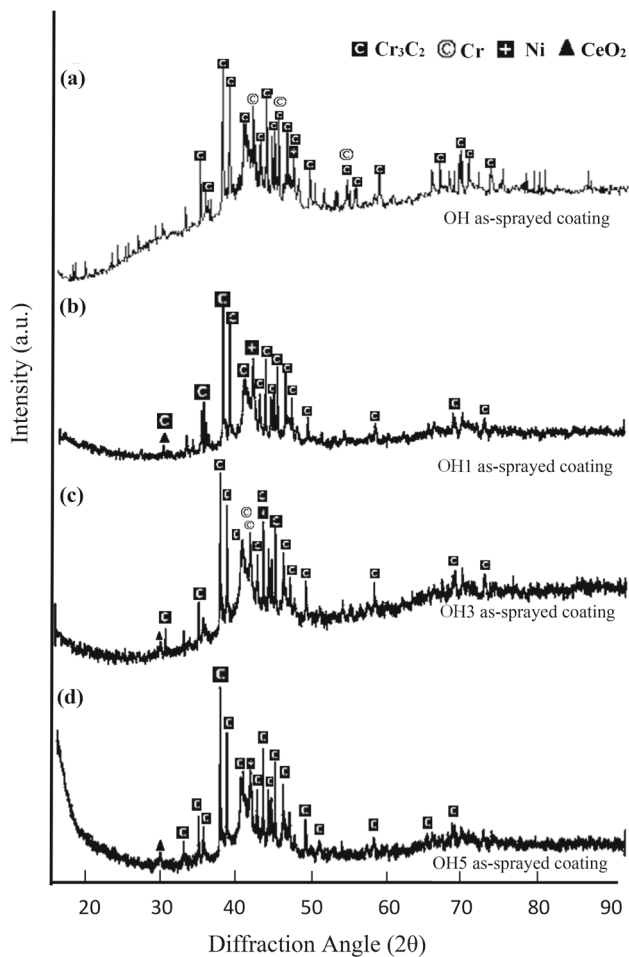
The surface roughness of the as-deposited coatings was determined to be in the range of 4.314–5.792 μm. The H5 coating modified with 1.2wt-% of CeO<sub>2</sub> particles shows minimum surface roughness (4.314 μm) than its counterparts, whereas the surface roughness for H3 and H1 were measured as 4.648 μm and 4.832 μm, respectively. Surface roughness measured for conventional coating (OH) is 5.792 μm. The above variation in surface roughness is due to un-melted and semi-melted particles on the surface of the TP347H steel substrate (Zhang et al. 2007).

#### 3.1.1 Surface morphology

The SEM/EDS analysis of HVOF as-sprayed conventional (OH) and ceria modified (OH1, OH3, and OH5) coatings is depicted in Fig. 3. All the HVOF sprayed coatings show dense microstructure having melted and semi-melted particles. The coating binder (NiCr) matrix is confirmed from SEM images, which is light grey in colour, whereas dark grey colour shows carbide particles of the coatings. In addition, Small white colour particles of CeO<sub>2</sub> can be seen on the OH1, OH3, and OH5 coatings surface. In the case of OH1 coating, surface morphology shows fully melted particles as compared to OH3 and OH5 coatings, which might be due to the lower ratio of CeO<sub>2</sub> in the conventional carbide coating. However, it is noted that the addition of CeO<sub>2</sub> greater than a critical value, does not affect the coating microstructure, as shown in Fig. 3d. The above fact of the higher ratio of RE element cannot improve the microstructure is confirmed from coatings microhardness (Hv), and micro-porosity results. Liang et al. (2016) and Cai et al. (2018) reported that when the addition of Ce is high, it loosens the adhesion of splat particles

**Fig. 3** FESEM/EDS spectrum of as-sprayed **a** OH coated, **b** OH1 coated, **c** OH3 coated, **d** OH5 coated substrate steels





**Fig. 4** XRD Analysis of **a**  $\text{CeO}_2$  powder, **b**  $\text{Cr}_3\text{C}_2$ –NiCr powders, and HVOF as-sprayed, **c** OH coated, **d** OH1 coated, **e** OH3 coated, and **f** OH5 coated substrate steels

due to entrapped gases/slag and impurities from the molten pool.

### 3.1.2 XRD analysis

XRD spectrums of HVOF as-sprayed OH, OH1, OH3, and OH5 coatings are shown in Fig. 4a–d. In OH coating (Fig. 4a), prominent peaks of  $\text{Cr}_3\text{C}_2$ ,  $\text{Cr}_7\text{C}_3$ , and NiCr were observed by XRD analysis. Whereas, in ceria-modified OH1, OH3, and OH5 coatings, significant peaks of  $\text{Cr}_3\text{C}_2$  and NiCr along with  $\text{CeO}_2$  were observed as shown in Fig. 4b–d. The amount of  $\text{CeO}_2$  is too small for producing phases with high intensity, so minute peaks were observed for all the ceria added coatings.

## 3.2 Oxidation kinetics



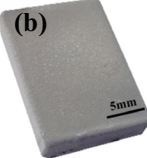

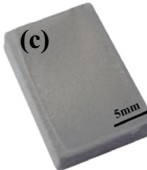
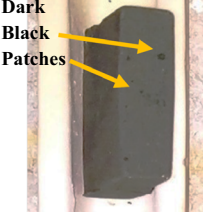
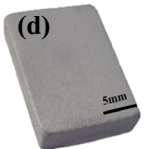

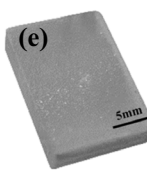
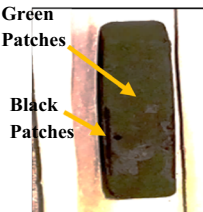
### 3.2.1 Visual remarks

The macro images of the base (TP347H) steel and OH, OH1, OH3, and OH5 coated samples after subjected to oxidation at 750 °C for 50 cycles are depicted in Fig. 5. All the observations about investigated samples have been written in tabulated form, as shown in Fig. 5. The bare steel experienced change in colour during the cyclic study, which might be due to the formation of oxide scale, as a result of which sample also experienced a gain in weight. However, no spallation of oxide scale is observed might be due to the presence of chromium in the base matrix.  $\text{Cr}_3\text{C}_2$ –NiCr coating (OH) experienced the formation of green and white patches on the dark grey surface of the sample. Among the cerium doped samples, OH5 coating experienced a change in colour from dark grey to greenish along with spallation of oxide scale. Similarly, the ceria added OH3-coated sample exhibited dark grey with greenish patches and black dots on the coating surface. During the cyclic research, no spallation of OH3-coated steel was found. OH1-coated steel shows white colour patches on a dark greyish surface, transforming into black after the ninth cycle in an oxidizing environment.

### 3.2.2 Weight gain data

From Fig. 6, it is observed that base steel has gained maximum weight, indicating poor oxidation resistance. The OH-coated sample indicated lower weight gain than base steel, suggesting towards protective nature of the coating. The addition of cerium (0.4 wt-%) to  $\text{Cr}_3\text{C}_2$ –NiCr coating further enhance the protective behaviour of coating and has gained minimum weight among the samples under study. However, doping of  $\text{Cr}_3\text{C}_2$ –NiCr coating with a higher weight percentage (1.2wt-%) of cerium could not improve the performance of the conventional coating. For the bare TP347H steel, the weight change after the end of 50<sup>th</sup> cycle is 6.102 mg/cm<sup>2</sup>, whereas the weight gain for OH, OH1, OH3, and OH5 coated samples is 3.748 mg/cm<sup>2</sup>, 1.079 mg/cm<sup>2</sup>, 2.054 mg/cm<sup>2</sup>, and 3.363 mg/cm<sup>2</sup>, respectively. For the OH1-coated sample, the weight gain was rapid during the initial cycle of the study. Afterward, it attains a steady-state, suggesting the rapid formation of oxides. The rapid development of the oxide layer may be due to the presence of Ce (0.4 wt-%) in the conventional coating. Rare earth element (Ce) acts as nucleation sites for the oxide layer, which reduces the distance of neighbouring oxide grains, resulting in smaller oxide gain size.

Subsequently, the protective oxide layer developed in a shorter time, which helps in achieving rapid steady-state conditions. Furthermore, a smaller oxide gain size improves the plasticity and adhesion of the oxide layer (Wang and Szpunar 2017). Low performance of OH5-coated steel might be due

Sample	Before Oxidation	After Oxidation	Observations
Bare			<ul style="list-style-type: none"> <li>• 5<sup>th</sup> Cycle Dark Greyish with brown patches</li> <li>• 25<sup>th</sup> Cycle Blackish with blue shining points</li> <li>• 50<sup>th</sup> Cycle Blackish with dark patches</li> <li>• Weight gained without spallation</li> </ul>
OH			<ul style="list-style-type: none"> <li>• 5<sup>th</sup> Cycle Dark Greyish with white patches</li> <li>• 25<sup>th</sup> Cycle Dark Greyish with green and white patches</li> <li>• 50<sup>th</sup> Cycle Dark Greyish with green and white patches</li> <li>• Weight gained with minor crack and spallation of oxide scale with powder type particles</li> </ul>
OH1			<ul style="list-style-type: none"> <li>• 5<sup>th</sup> Cycle Dark Greyish with white patches</li> <li>• 25<sup>th</sup> Cycle Dark Greyish with black dots</li> <li>• 50<sup>th</sup> Cycle Dark Greyish with more black dots</li> <li>• Weight gained without spallation</li> </ul>
OH3			<ul style="list-style-type: none"> <li>• 5<sup>th</sup> Cycle Dark Greyish with green patches</li> <li>• 25<sup>th</sup> Cycle Dark Greyish with green patches</li> <li>• 50<sup>th</sup> Cycle Dark Greyish with green patches and black dots</li> <li>• Weight gained without spallation</li> </ul>
OH5			<ul style="list-style-type: none"> <li>• 5<sup>th</sup> Cycle Light Greyish with green patches</li> <li>• 25<sup>th</sup> Cycle Dark Greyish with more green patches</li> <li>• 50<sup>th</sup> Cycle Greenish with black patches</li> <li>• Weight gained with spallation</li> </ul>

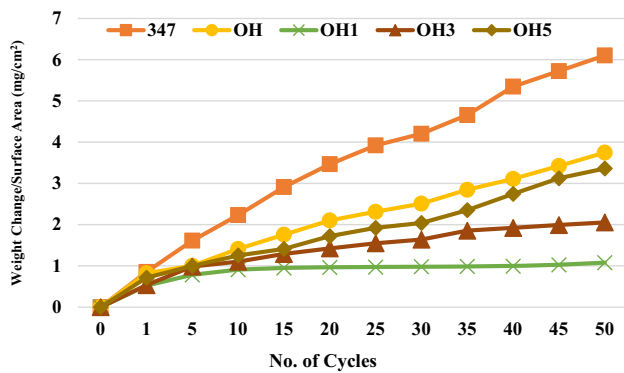
**Fig. 5** Macrograph of, **a** bare, **b** OH coated, **c** OH1 coated, **d** OH3 coated, and **e** OH5-coated steel after subjected to cyclic oxidation in air at 750 °C for 50 cycles

to higher wt-%age of Ce doped in the conventional coating. A higher Ce (1.2 wt-%) ratio in  $\text{Cr}_3\text{C}_2\text{-NiCr}$  coating may increase the porosity due to the oxygen concentration effect of rare earth elements. Various authors reported that the Ce element acts as a source of oxygen due to its characteristic to release/absorb oxygen (Patil et al. 2006; Babu et al. 2009; Choudhury et al. 2015). Excess air entrapping towards coating may increase the porosity of coating, which reduces its compactness, and hence oxidizing species travel towards substrate material (Schmucker et al. 2016).

### 3.2.3 Surface analysis

Figure 7 illustrates the 50th cycle surface morphology of uncoated and HVOF-coated substrates after the exposure of oxidation in air at 750 °C. Figure 7a SEM/EDS represents the flaky structure from the surface, which is primarily composed of Fe along with Cr, Ni and O, suggesting the formation of oxides of these elements. In the EDS analysis (Fig. 7b) of the OH-coated steel reveals the oxide scale rich in Cr and Ni along with O, indicating the surface mainly covered with  $\text{Cr}_2\text{O}_3$ ,  $\text{NiCr}_2\text{O}_4$ , which is validated by XRD results (Fig. 8b).





**Fig. 6** Weight change vs number of cycles plots for bare and HVOF sprayed conventional and modified  $\text{Cr}_3\text{C}_2$ -NiCr coatings with different concentrations of  $\text{CeO}_2$  particles after subjected to air oxidation at  $750^\circ\text{C}$  for 50 cycles

Another phase,  $\text{Cr}_3\text{C}_2$ , depicts the basic structure of the coating, whereas the  $\text{Cr}_{23}\text{C}_6$  phase arises after the decomposition of  $\text{Cr}_3\text{C}_2$  at  $750^\circ\text{C}$ . In the EDS analysis (Fig. 7c–e) of ceria modified OH1, OH3, and OH5 coated steel exhibits the presence of O, Cr, Ni and Ce, suggest the formation of oxides of these elements. Moreover, EDS analysis Fig. 7c–e indicated that the amount of Cr along with Ni first decreases with lower concentration of Ce and it increases after the increase in the concentration of Ce. From the above results, it is observed that the lower ratio of RE element (Ce) retard the regular growth of oxide (Cr) layer.

### 3.2.4 XRD analysis

Phase identification for bare and coated samples after being exposed to oxidation in air at  $750^\circ\text{C}$  for 50 cycles (Fig. 8) has been done using XRD analysis. In all the coated samples, chromium oxide ( $\text{Cr}_2\text{O}_3$ ), chromium carbide ( $\text{Cr}_3\text{C}_2$ ), and nickel–chromium oxide ( $\text{NiCr}_2\text{O}_4$ ) are observed as the typical (significant) phases. Whereas,  $\text{Cr}_{23}\text{C}_6$  peaks exist only in OH and OH3-coated steel. XRD profiles for the ceria modified (OH1, OH3, and OH5)  $\text{Cr}_3\text{C}_2$ -NiCr-coated steel shows the other phases than the above reported are  $\text{CeO}_2$ ,  $\text{Ce}_2\text{O}_3$ , and  $\text{CeCrO}_3$  phases, which may develop after the chemical reaction between Cr and Ce in the presence of O. In the case of bare steel,  $\text{Fe}_2\text{O}_3$  and  $\text{NiFe}_2\text{O}_4$  are identified as the significant phases and  $\text{NiCr}_2\text{O}_4$  as the minor phase.

### 3.2.5 Cross-sectional analysis

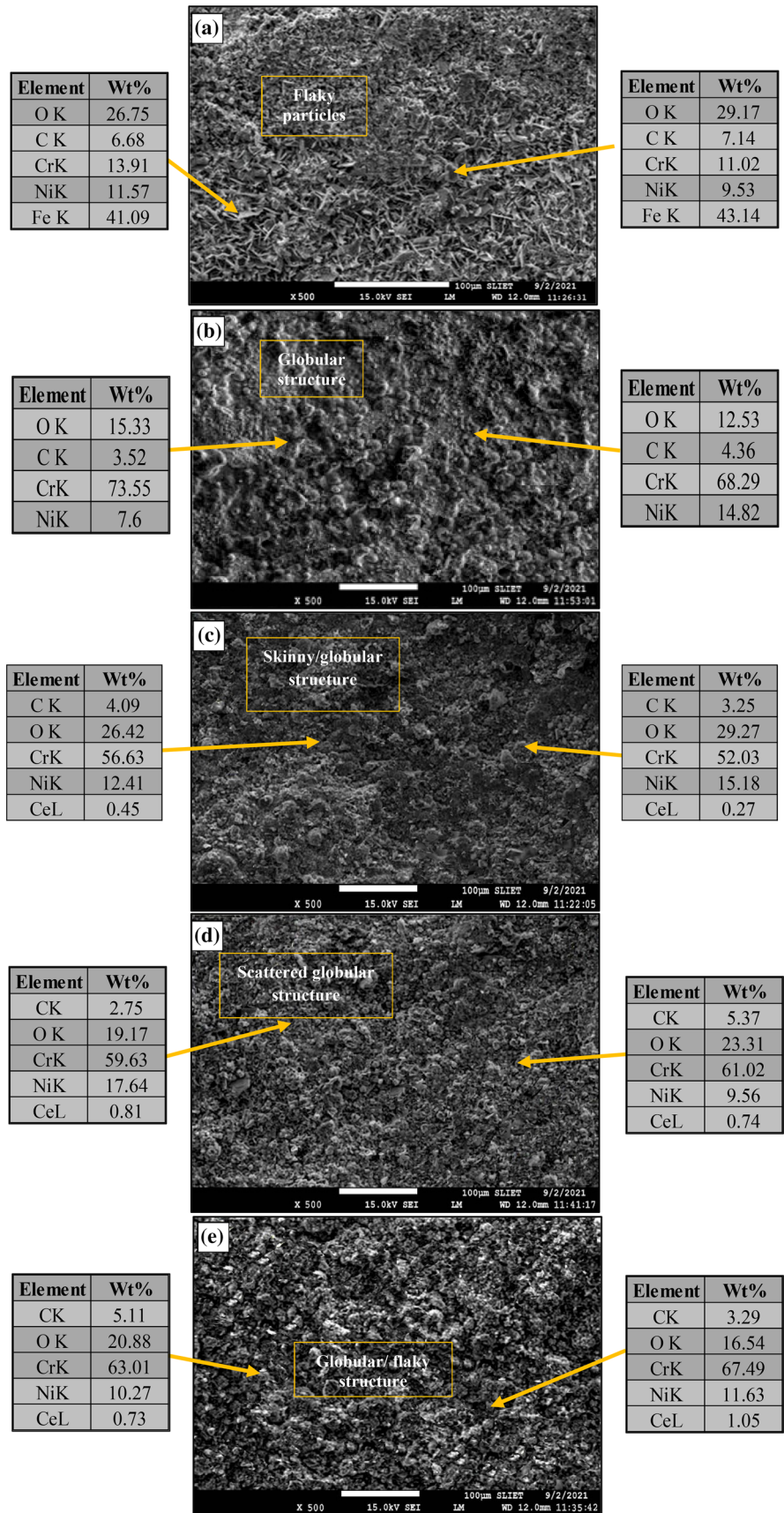
EDS cross-sectional point analysis Fig. 9 has been done for the bare steel after oxidation in air at  $750^\circ\text{C}$  for 50 cycles. Figure 9 shows a thin oxide scale of about 50 microns produced on the surface of the oxidized TP347H steel. Points 1, 2, and 3 indicate compositional elements of the bare steel. Points 4 and 5, which are taken on the oxide scale, show

the existence of oxygen and iron as the main element along with some nickel and chromium, which demonstrated the possibility of the formation of oxides of iron, nickel, and Cr. Elemental cross-sectional point analysis has been done for the HVOF sprayed OH-coated steel after oxidation at  $750^\circ\text{C}$  for 50 cycles. OH-coated TP347H steel shows the formation of thin ( $50\ \mu\text{m}$ ) and compact oxide scale as revealed from cross-sectional SEM micrographs as shown in Figs. 10a and 17d. Point 1 indicates the substrate steel without any oxygen. This shows that the substrate remained unreacted with the surrounding environment. Points 2–6 indicate the presence of a substantial amount of Cr and Ni along with carbon, which shows the basic composition of the coating. At Point 6, a higher concentration of nickel, chromium, and oxygen is seen, indicating the formation of oxides of Ni and Cr on the top of the surface of the oxidized OH sample. EDS analysis across the cross-section of the ceria-modified OH1, OH3, and OH5 coatings after oxidation in air at  $750^\circ\text{C}$  for 50 cycles are depicted in Fig. 10b–d, respectively. Similarly, the thickness of the oxide scales is estimated from the above cross-sectional SEM micrographs as well as from the cross-sectional SEM at the  $2000\times$  scale, as depicted in Fig. 17ac. Ceria modified OH1-coated sample exhibited the formation of a thin ( $20\ \mu\text{m}$ ), compact, and crack-free oxide scale after oxidation in air at  $750^\circ\text{C}$ . Points 2 to 6 depict the presence of Cr and Ni along with a minor amount of Ce. On the top of the oxide scale (point 7), chromium, nickel, and oxygen are observed in a significant amount along with Ce, which indicates the possibility of forming oxides of observed elements. In the case of OH3-coated TP347H steel, a thin ( $35\ \mu\text{m}$ ) oxide layer with scattered edges was observed from the SEM/EDS point analysis (Fig. 10c). Points 2, 3, 4, 5, and 6, which lie inside the coating, show the presence of Cr and Ni, along with minor amounts of Ce distributed throughout the coating. At point 7, nickel, chromium, and oxygen are seen with a minor presence of Ce, which indicates the formation of oxides of these elements. An EDS point analysis Fig. 10d observed a thin ( $45\ \mu\text{m}$ ) oxide layer with spallation for OH5-coated TP347H steel after oxidation in air at  $750^\circ\text{C}$ . Point 1 confirms the structure of substrate steel, whereas points 2 to 6 reveal the composition of the coating. Point 7 on the top of the surface suggests the chances of oxides of Ni and Cr along with Ce.

### 3.2.6 Mapping analysis

Figure 11 shows an X-ray map analysis of bare TP347H steel exposed to cyclic air oxidation after 50 cycles at a temperature of  $750^\circ\text{C}$ . According to the compositional image, the primary oxidation occurs at the substrate/scale interface, which develops a brittle, weakly connected oxide scale of iron. In addition to iron, austenite steel is composed of Cr and Ni with some minor elements, suggesting the formation

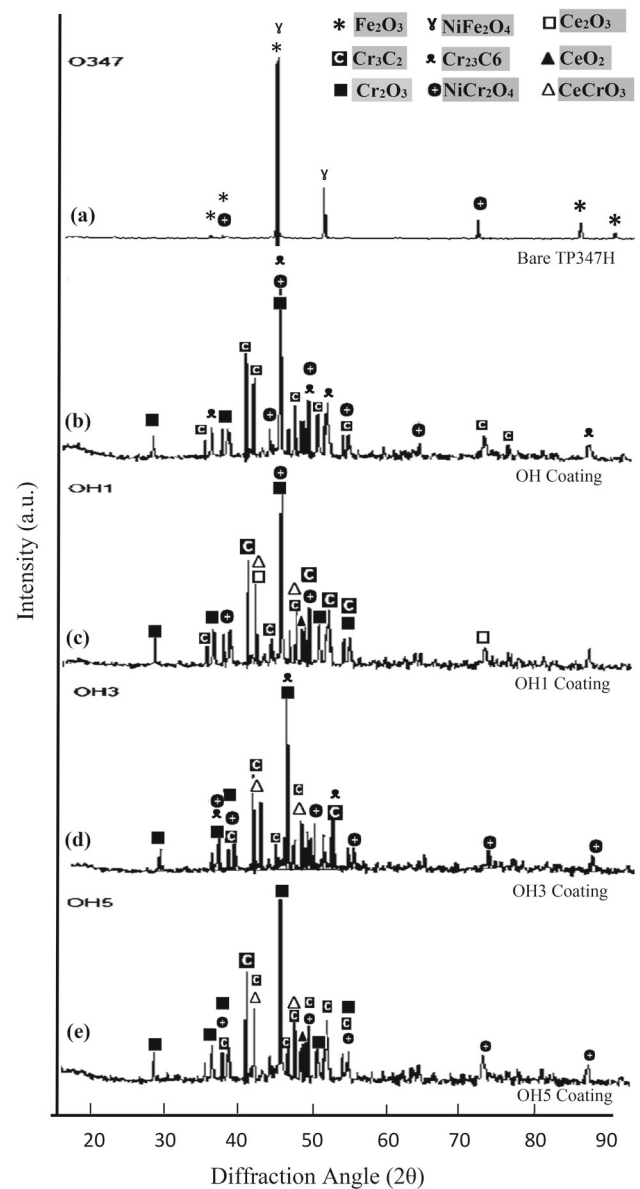
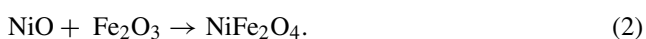
**Fig. 7** SEM/EDS surface analysis for, **a** bare, **b** OH coated, **c** OH1 coated, **d** OH3 coated, and **e** OH5-coated steel after subjected to cyclic oxidation in air at 750 °C for 50 cycles



of oxides of these elements. X-ray mapping of OH-coated TP347H steel (Fig. 12) after oxidation in air at 750 °C for 50 cycles indicated the formation of a thin oxide scale, which contains mainly chromium, nickel, and oxygen along with carbon. The formation of a dense layer of chromium oxide with spinels of Ni–Cr does not allow any further diffusion, thereby slowing down the oxidation rate. Figures 13, 14 and 15 illustrate the elemental mapping analysis for ceria-modified OH1, OH3, and OH5 coated TP347H steel after oxidizing in the air environment at 750 °C for 50 cycles. The composition images indicated that all the ceria-added coatings successfully protect the base metal after developing the oxide scale on the top of the coatings, which is primarily composed of Cr and Ni, along with Ce distributed throughout the coatings. In addition, no diffusion of oxygen was observed after the oxide scale developed on the top of the surface of coatings. But in the case of OH5-coated steel, coating spallation (tiny particles) was observed during the oxidation study, which might be due to the higher amount of ceria added in Cr<sub>3</sub>C<sub>2</sub>–NiCr coating.

## 4 Discussion

Under the cyclic oxidation study, bare steel (TP347H) experienced maximum weight gain (6.102 mg/cm<sup>2</sup>), indicating the low oxidation resistance of base steel. The oxide scale formation is also revealed during visual observations in which the sample experienced a change in colour from metallic grey to black with dark patches during the cyclic study. Some of the bright blue spots were observed after the 4th cycle, suggesting the formation of oxides and spinels of Fe, Cr, and Ni (Fan et al. 2020). Weight gain analysis Fig. 6 of bare TP347H steel showed a significant increase in weight during oxidation cycles, which might be due to the formation of oxides of basic elements (Iron) present in the bare steel. At high temperature in an oxidizing environment, TP347H steel develops a fragile oxide layer, which was comprised of Fe<sub>2</sub>O<sub>3</sub> (Haematite), NiFe<sub>2</sub>O<sub>4</sub> (Nickel–Magnetite), and NiCr<sub>2</sub>O<sub>4</sub> (Nickel–Chromium oxide), as revealed by XRD analysis (Fig. 6a). Iron has a greater affinity for oxygen than other alloying elements, resulting in iron diffusing quicker than other constituents and forming an oxide layer (Fe<sub>2</sub>O<sub>3</sub>) of iron (Nyadongo et al. 2021). As the bare steel consists of alloying elements (Ni, Cr) along with iron, so diffusion–reaction is continuous under long term exposure, which creates more compounds due to the following reactions:

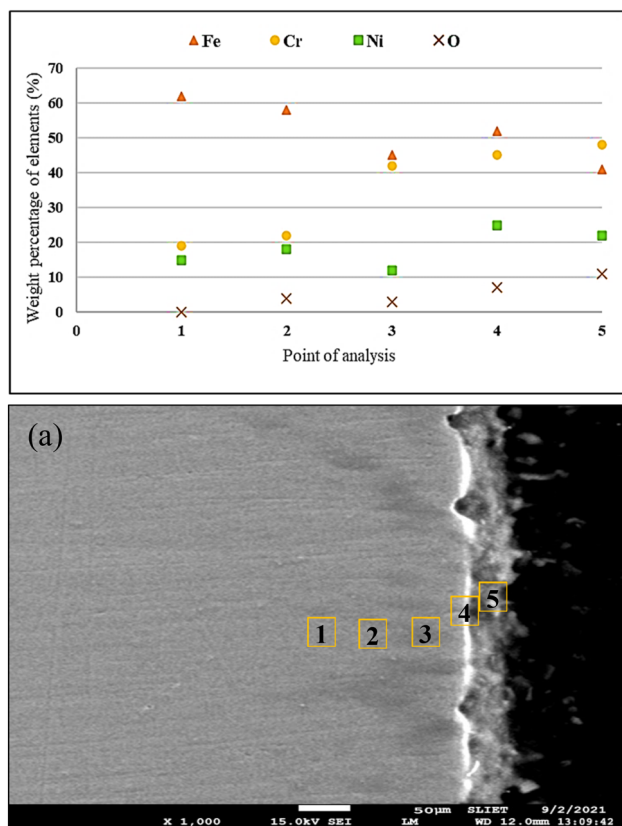


**Fig. 8** XRD Analysis of, **a** bare and HVOF coated, **b** OH, **c** OH1, **d** OH3, and **e** OH5 samples after oxidation at 750 °C for 50 cycles

After diffusion of iron towards the top of the surface, it further reacts with nickel in the presence of the surrounding environment, which generates another compound of Ni and Fe. Similarly, NiCr<sub>2</sub>O<sub>4</sub> spinels were detected by XRD peaks during oxidation study, which might be due to outward diffusion and reaction of NiO and Cr<sub>2</sub>O<sub>3</sub> to form NiCr<sub>2</sub>O<sub>4</sub> spinels (Shi et al. 2012; Ding et al. 2015; Chen et al. 2020a).

EDS and X-ray mapping analysis of bare steel shows oxide scale primarily composed of iron and spinels of Ni and Cr as shown in Figs. 9 and 11, respectively. No spallation and sputtering were observed during the oxidation study for TP347H steel, as shown in Fig. 5a, which might be due to the significant presence of Cr (17.53%) in the substrate material (Gheno





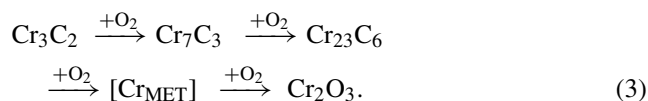
**Fig. 9** EDS point analysis across the cross-section of bare TP347H substrate steel after oxidation in air at 750 °C for 50 cycles

et al. 2012; Thakare et al. 2019; Veselkov et al. 2021). Various authors reported that the presence of Cr in the base metal produces oxides and spinels (Eq. 2) of the chromium due to its more negative Gibbs free energy, as illustrated by the Ellingham diagram. The initiation of reaction in the presence of oxygen depends upon the negativity of Gibbs free energy (thermodynamic driving force) available to carry out the reaction. However, in the present study oxide scale is mainly composed of  $\text{Fe}_2\text{O}_3$ , which affects the stability of chromium and its spinels (Col et al. 2017). Oxides of iron are reported to be non-protective due to the porous structure through which oxidizing species travel towards base metal, and deterioration of metal takes place (Habib et al. 2011; Chatha et al. 2012; Huang et al. 2020). Figure 16 represents the schematic diagram of the oxidation mechanism that proceeds through the TP347H steel substrate after subjecting to the oxidizing environment at 750 °C for 50 cycles.

In the case of HVOF-coated samples, a dark grey oxide scale appeared all over the surface, which get intensified with the passage of cycles. After a few cycles, green colour oxide also starts appearing on the scale. The presence of dark grey colour oxide indicates the formation of chromium oxide, and green colour suggests NiO, as reported by Kaur et al.

(2009). As-sprayed ceria-doped  $\text{Cr}_3\text{C}_2$ -NiCr coating indicated a better value of microhardness than the conventional coating, which might be due to grain refinement (heterogeneous nucleation) and reduction in microporosity due to a decrease in interfacial energy and surface tension between crystal nucleus and the melted feedstock powder during coating deposition (Wei et al. 2014; Saladi et al. 2015; Shu et al. 2020; Wu et al. 2020).

The HVOF sprayed  $\text{Cr}_3\text{C}_2$ -NiCr coating (OH) successfully enhanced the oxidation resistance of austenite (TP347H) steel after developing an oxide scale, which primarily comprised of  $\text{Cr}_2\text{O}_3$ ,  $\text{Cr}_{23}\text{C}_6$ ,  $\text{Cr}_3\text{C}_2$ , and  $\text{NiCr}_2\text{O}_4$ , phases as confirmed by XRD analysis (Fig. 8b). Weight change data also illustrate that the  $\text{Cr}_3\text{C}_2$ -NiCr-coated sample gained a higher weight ( $3.748 \text{ mg/cm}^2$ ) than ceria added coatings. The oxide scale formation is also validated by the change in colour of the OH-coated sample from light grey to dark grey, along with dark green patches. Dark grey colour on the coating surface suggests  $\text{Cr}_2\text{O}_3$ , and dark green colour suggests towards NiO, as reported by (Liu et al. 2020a). Due to high thermal stability, the  $\text{Cr}_2\text{O}_3$  compound protects the base metal from oxidizing species after the development of a thick and continuous oxide layer as depicted in SEM/EDS analysis (Fig. 10a) and X-ray map analysis (Fig. 12). The formation of  $\text{Cr}_2\text{O}_3$  might be due to the reaction of Cr and oxidation of  $\text{Cr}_3\text{C}_2$  in various steps resulting in the development of  $\text{Cr}_{23}\text{C}_6$  or  $\text{Cr}_2\text{O}_3$  (Qu et al. 2008; Mittal et al. 2014).

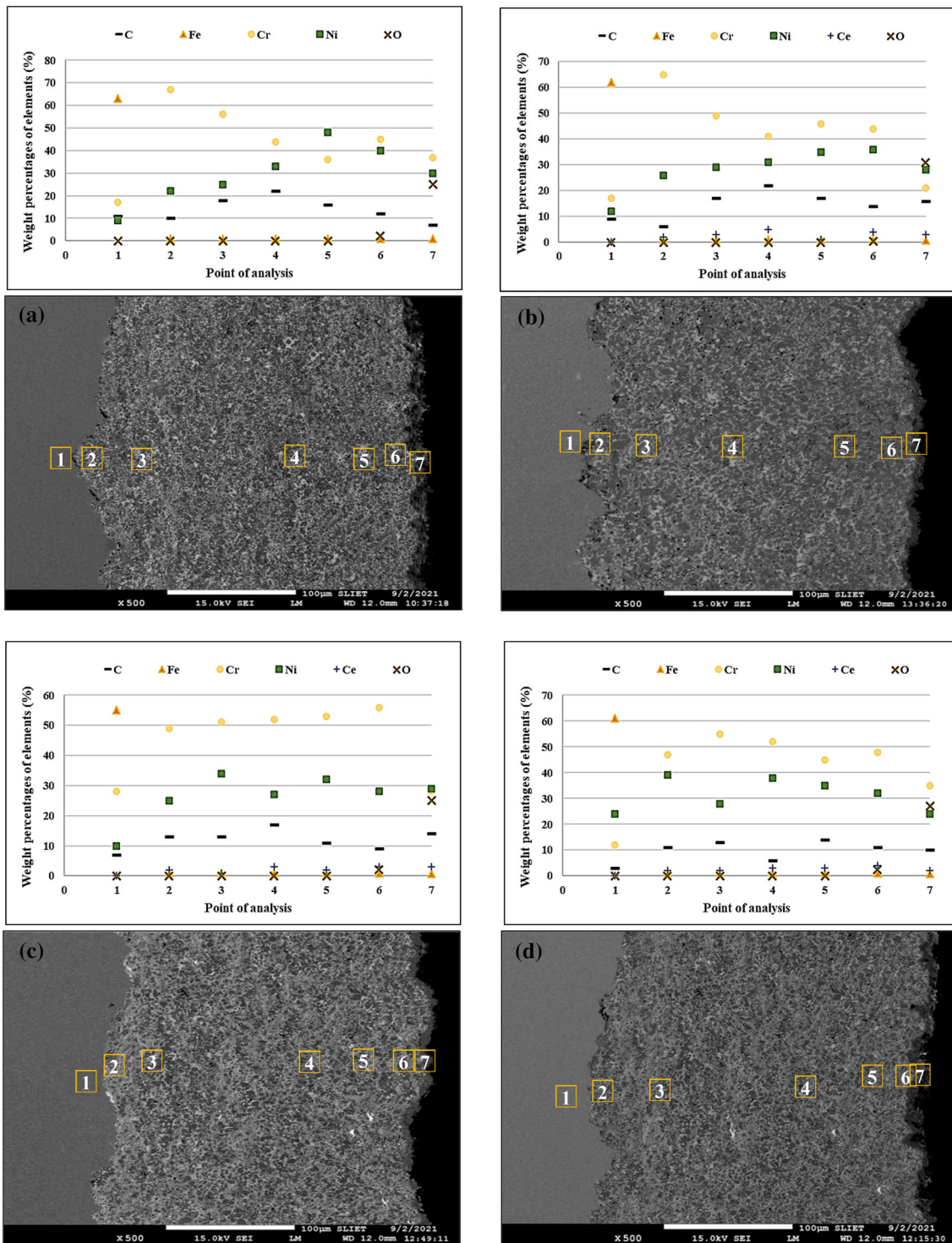


According to the Cr-C-O phase diagram of carbides at 1 atm pressure,  $\text{Cr}_{23}\text{C}_6$ ,  $\text{Cr}_7\text{C}_3$ ,  $\text{Cr}_3\text{C}_2$ , and  $\text{Cr}_2\text{O}_3$  may coexist at 750 °C. The above chromium carbide compounds with higher carbon percentages are more stable. The  $\text{Cr}_{23}\text{C}_6$  compound may react with diffusible carbon at the  $\text{Cr}_2\text{O}_3/\text{Cr}_{23}\text{C}_6$  interface to form  $\text{Cr}_7\text{C}_3$  or  $\text{Cr}_3\text{C}_2$  via the reactions listed below (Wu et al. 2015).



Furthermore, the spinels of Ni and Cr ( $\text{NiCr}_2\text{O}_4$ ) also facilitated higher oxidation resistance due to their low diffusion coefficient than parental oxides (Nyadongo et al. 2021). However, minor cracks with spallation of tiny particles were noticed in the case of OH-coated sample during the cyclic study. Due to thermal fluctuations (heating/cooling), the plasticity of the oxide scale is directly affected by stress generated within the oxide scale (song et al. 2011). Due to these

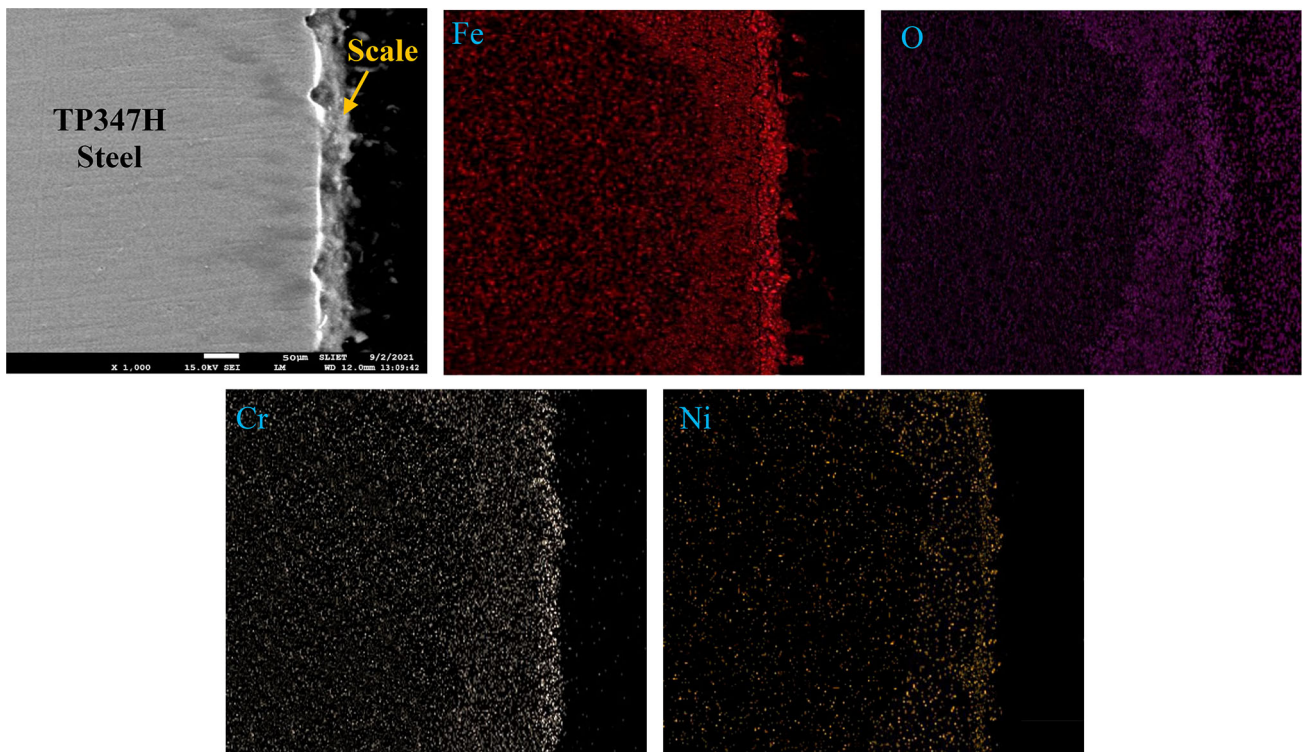




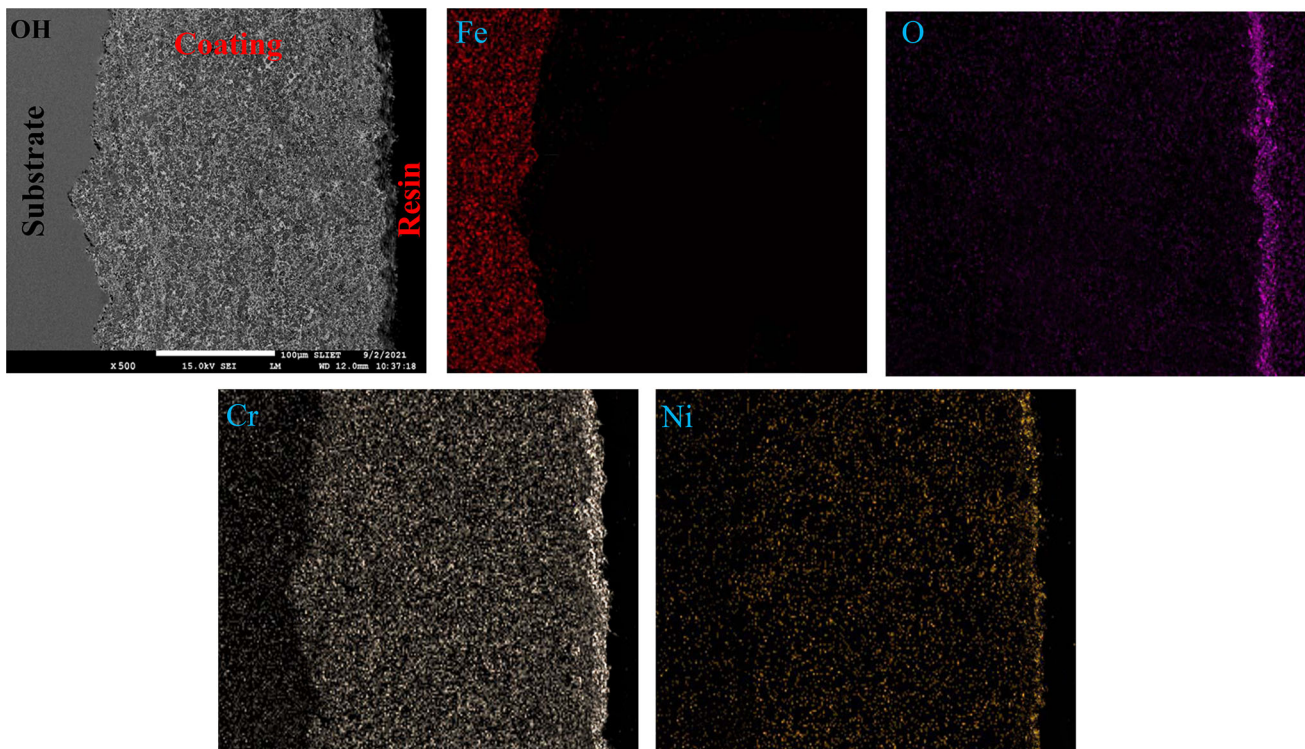
**Fig. 10** EDS point analysis across the cross-section of **a** OH, **b** OH1, **c** OH3, and **d** OH5-coated steel after oxidation in air at 750 °C for 50 cycles

stresses (compressive/tensile), deformation (cracks, spallation, delamination) occurs in the oxide scale, which helps in releasing the stresses within an oxide layer (Kitamura et al. 2019; Kumar et al. 2019a). Ceria modified OH1-coated steel performed better under cyclic oxidation with no cracking

& spallation observed throughout the 50 cycles. From the weight change chart (Fig. 6), It is estimated that OH1-coated sample experienced minor weight gain ( $1.079 \text{ mg/cm}^2$ ) during initial cycles, which might be due to the rapid formation of the oxide layer of chromium and nickel along with cerium



**Fig. 11** Composition image and X-ray mapping analysis across the cross-section of bare TP347H substrate steel after air oxidation at 750 °C for 50 cycles



**Fig. 12** Composition image and X-ray mapping analysis across the cross-section of OH-coated steel after air oxidation at 750 °C for 50 cycles



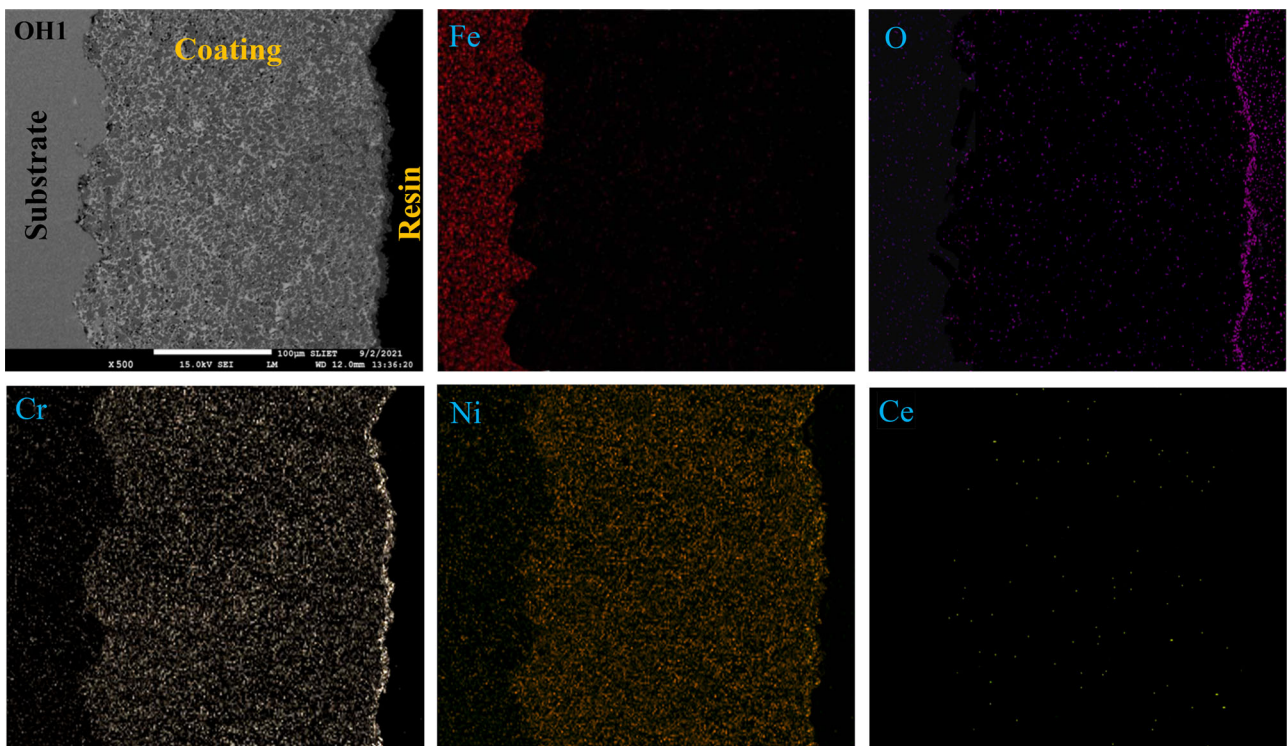


Fig. 13 Composition image and X-ray mapping analysis across the cross-section of OH1-coated steel after air oxidation at 750 °C for 50 cycles

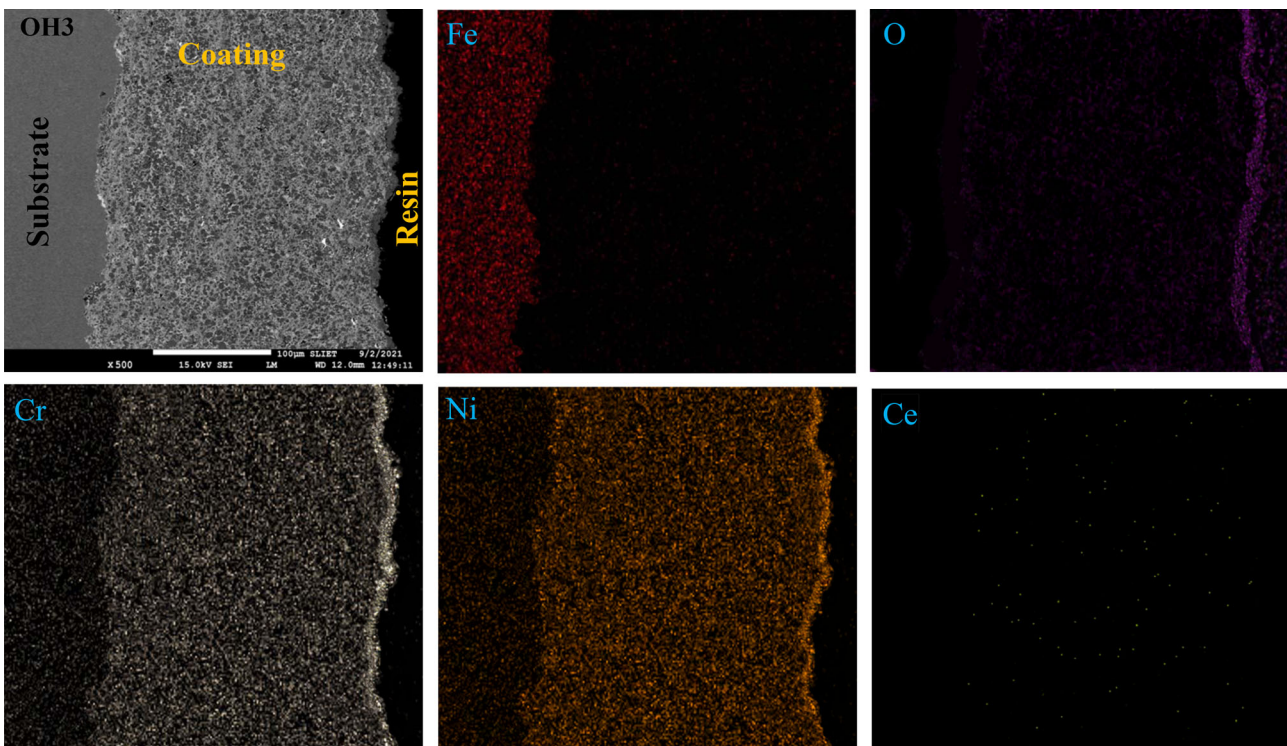
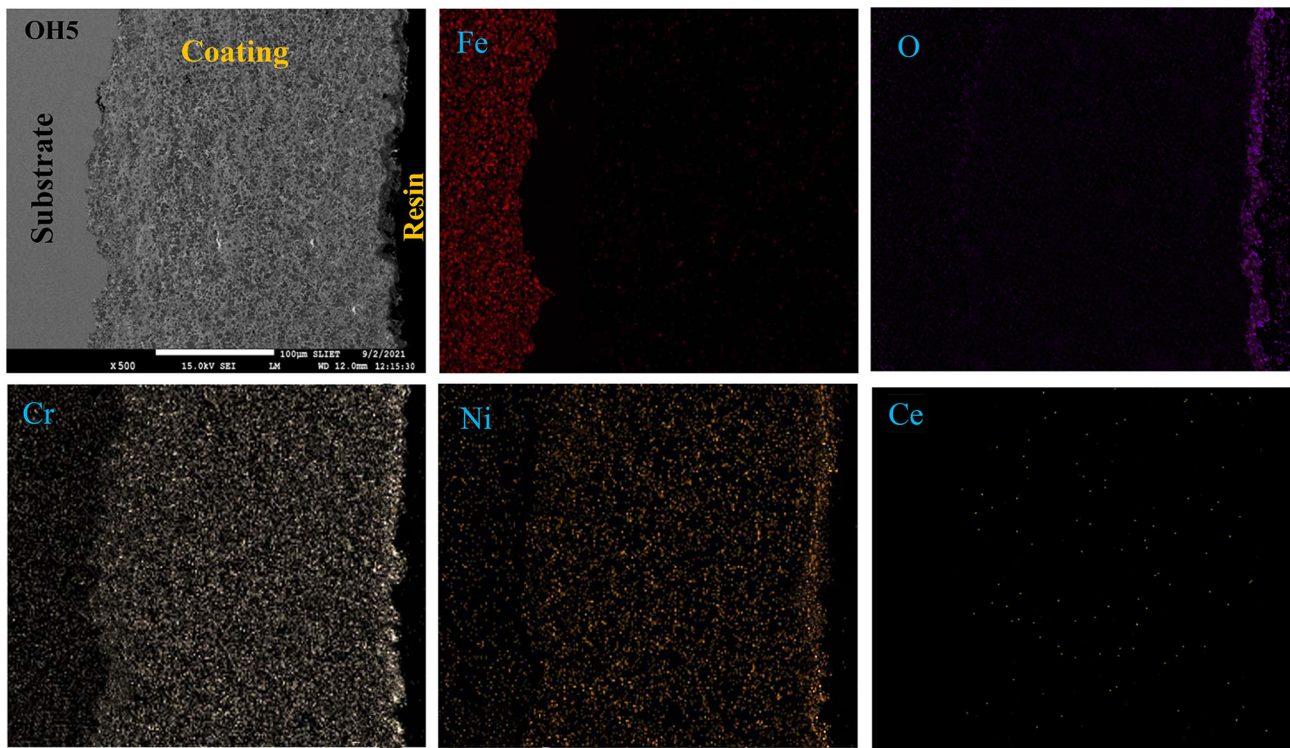
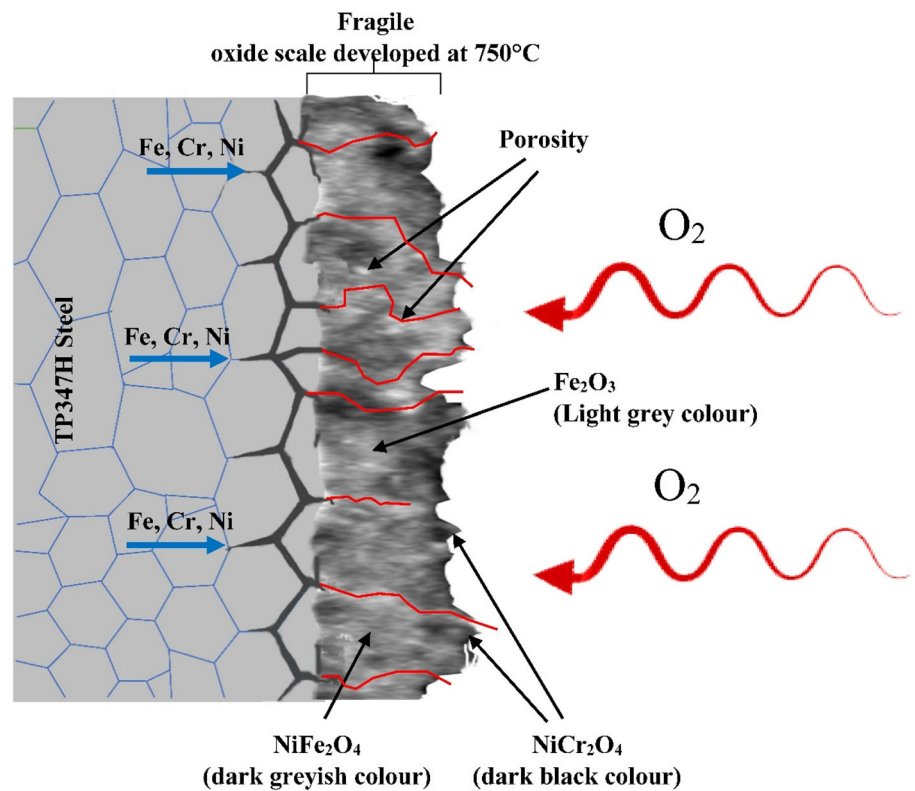


Fig. 14 Composition image and X-ray mapping analysis across the cross-section of OH3-coated steel after air oxidation at 750 °C for 50 cycles

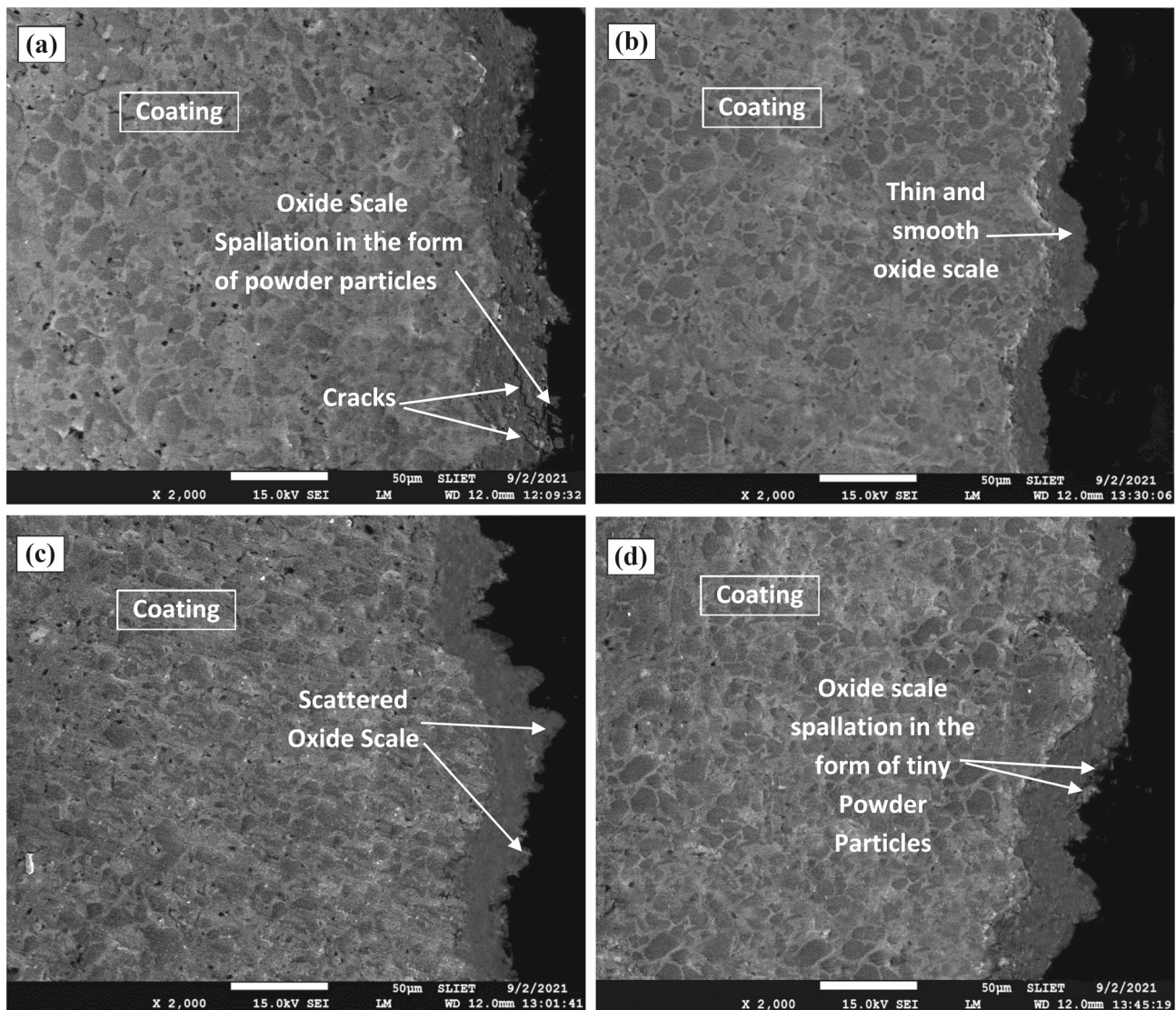


**Fig. 15** Composition image and X-ray mapping analysis across the cross-section of OH5-coated steel after air oxidation at 750 °C for 50 cycles

**Fig. 16** Schematic diagram represents oxidation mechanism bare TP347H after subjecting to the oxidizing environment at 750 °C for 50 cycles



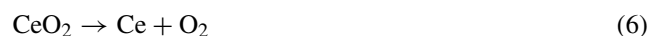




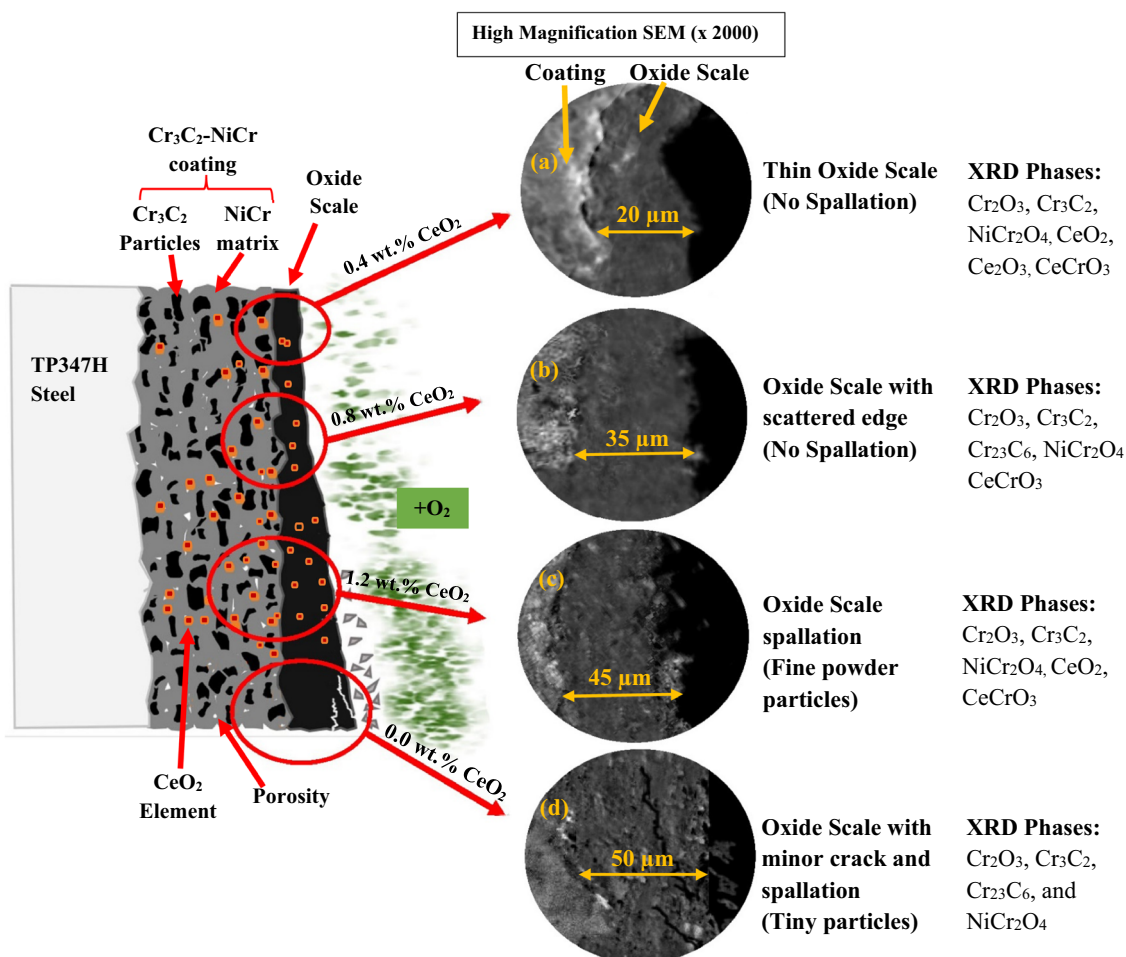
**Fig. 17** Oxidation analysis at higher magnification across the cross-section of, **a** OH, **b** OH1, **c** OH3, and **d** OH5-coated steel after 50 cycles at 750 °C

on the surface of the coating, as seen in X-ray mapping analysis (Fig. 12). Figure 8c shows the XRD analysis of the oxidized OH1-coated sample, which indicates the formation of  $\text{Cr}_2\text{O}_3$  and  $\text{NiCr}_2\text{O}_4$  as major phases along with  $\text{Cr}_3\text{C}_2$ ,  $\text{CeO}_2$ ,  $\text{Ce}_2\text{O}_3$ , and  $\text{CeCrO}_3$  as the minor phases. The presence of  $\text{CeO}_2$ ,  $\text{Ce}_2\text{O}_3$ , and  $\text{CeCrO}_3$  phases might increase the grain boundaries (GB) area after decreasing grain size due to heterogeneous nucleation, which improves the diffusion of chromium through these grain boundaries (Qu et al. 2008; Kadgaye et al. 2021). The above improvement decreases the critical concentration of chromium to form the  $\text{Cr}_2\text{O}_3$  layer (Li et al. 2014). Once the protective layer forms on the surface of the coating, it achieves steady-state oxidation and impedes the diffusion of oxygen and other corroded species (Kamal and Sharma 2016; Shao et al. 2012; Sharma 2012;

Sharma et al. 2008). XRD identified peak of  $\text{CeO}_2$  element have characteristics to store/release  $\text{O}_2$  at high-temperature, resulting in decomposition of  $\text{CeO}_2$  (+ 4 oxidation state) to  $\text{Ce}_2\text{O}_3$  (+ 3 oxidation state) and oxygen (Botu et al. 2014; Liu et al. 2015). The expressions can be expressed as:

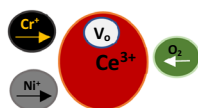


In the + 4-oxidation state, cerium has  $\text{Ce}^{4+}$  ions, and after conversion to + 3 oxidation state, its properties change to  $\text{Ce}^{3+}$  ions. When cerium changes from  $\text{Ce}^{4+}$  to  $\text{Ce}^{3+}$  state, resulting in oxygen vacancies formation (Wu and Lin 2014; Han et al. 2019). The Kroger–Vink notation can be used



### Summary:

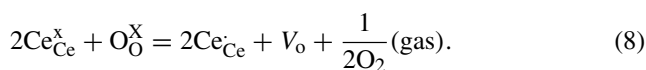
Figs a, b, and c Ce Mechanism



1. Cerium oxide in oxidation state (Ce<sup>3+</sup>) create hindrance (after grain boundary segregation) for the cations (Cr<sup>+</sup> and Ni<sup>+</sup>) and anions (O<sub>2</sub>) due to large ionic size, resulting in slow down the migration (diffusion) process.
2. Simultaneously, when CeO<sub>2</sub> decomposes to Ce<sub>2</sub>O<sub>3</sub> it releases oxygen and creates oxygen vacancies V<sub>o</sub>. The Cr<sup>+</sup> cations occupy these oxygen vacancies by the formation of CeCrO<sub>3</sub> phase.
3. Due to the above-proposed mechanisms, the thin and compact oxide layer developed inside rather than outside the coating, which acts as a barrier to oxidizing species.

**Fig. 18** Schematic diagram represents the oxidation mechanism of Cr<sub>3</sub>C<sub>2</sub>-NiCr coatings after the addition of different concentrations of CeO<sub>2</sub> particles

to express this reaction as (Thanneeru et al. 2007; Muhich 2017):

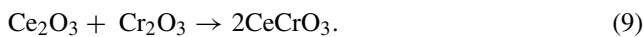


These oxygen vacancies play a vital role in mass diffusion. The defect of oxygen vacancies concentration depends on the dopant content and the degree of reaction (Esposito et al. 2013). The initial oxidation rate is determined by the migration of oxygen inward through the oxygen vacancies

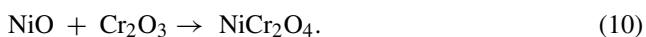
existing in the ceria modified coating at high temperatures. The availability of oxygen increases with the concentration (wt-%) of dopant in the coating at high temperature. The segregation of Ce (Ce<sup>3+</sup> and Ce<sup>4+</sup>) metal ions at grain boundaries of the Cr<sub>2</sub>O<sub>3</sub> layer limits chromium outward diffusion while boosting oxygen inward diffusion (Rahman and Jayaganthan 2016). Zinkevich et al. (2006), and Lone et al. (2019) reported that the ionic radius of cerium (Ce<sup>3+</sup> and Ce<sup>4+</sup>) is larger than Cr cations and Ni cations and from oxygen anions, which acts



as a barrier (hindrance) towards cation diffusion after segregating at grain boundaries resulting in a change in oxide growth mechanism by cation diffusion to anion diffusion. This is evident from the weight change graph (Fig. 6), which shows that adding CeO<sub>2</sub> to the Cr<sub>3</sub>C<sub>2</sub>–NiCr coating reduced weight gain. XRD profile (Fig. 8c) of OH1-coated steel further validates the above results after showing the CeCrO<sub>3</sub> phase in the spectrum. The above compound (CeCrO<sub>3</sub>) developed after the chemical reaction between Ce<sub>2</sub>O<sub>3</sub> and Cr<sub>2</sub>O<sub>3</sub> phases in the presence of oxygen (Shukla et al. 2009; Li et al. 2010; Siripongsakul et al. 2017). The expression of reaction can be written as:



The existence of the CeCrO<sub>3</sub> phase might be due to the segregation effect of cerium in grain boundaries of the Cr<sub>2</sub>O<sub>3</sub> layer (Li and Chen 2010; Kumar et al. 2014; Stefan et al. 2017). Due to the above change in the oxide growth mechanism, the vacancy (oxygen) formation inside the oxide layer (due to outward cation diffusion) decreases, improving the oxide layer's density (compactness). In the present study, a dense and thin oxide layer of Cr<sub>2</sub>O<sub>3</sub> was observed after adding minor wt-%age (0.4) of ceria in Cr<sub>3</sub>C<sub>2</sub>–NiCr coating, which protects the base TP347H steel from the oxidizing environment. Various authors (Kawamura et al. 1998; Yin et al. 2010; Colson et al. 1995; Kamal and Sharma 2016) have reported similar results of improving the microstructure of coatings after the addition of the Ce element. From the weight gain graph Fig. 6, it is observed that OH3-coated steel gained a higher weight (2.054 mg/cm<sup>2</sup>) than OH1 and OH-coated steel. The OH3 coating with 0.8 wt-% ceria provided superior protection to the base steel in the oxidizing environment at 750 °C for 50 cycles. The OH3-coated steel's XRD profile (Fig. 8d) confirmed the existence of basic, complicated, and combined oxides (spinels), including Cr<sub>2</sub>O<sub>3</sub>, Cr<sub>3</sub>C<sub>2</sub>, Cr<sub>23</sub>C<sub>6</sub>, Ni<sub>2</sub>Cr<sub>2</sub>O<sub>4</sub>, and CeCrO<sub>3</sub> spinels. The development of the Cr<sub>2</sub>O<sub>3</sub> layer might be due to a chemical reaction that occurred, as represented in Eq. 3, which provided better protection to the substrate material (Yu et al. 2020). In addition to the above oxides, NiCr<sub>2</sub>O<sub>4</sub> spinels also support the oxidation resistance, which developed after oxygen diffusion through NiO towards Cr<sub>2</sub>O<sub>3</sub> (Shi et al. 2020; Chen et al. 2020b). The expression can be written as:



The ceria-modified OH3 coating provided good oxidation resistance at 750 °C might be due to the dense and compact oxide scale of chromium oxide along with minor spinels of nickel and cerium as confirmed by X-ray mapping analysis (Fig. 14). OH3-coated steel indicated superior

protection from oxidizing species might be due to the segregated CeCrO<sub>3</sub> phase (Eq. 9) along the grain boundaries of the oxide scale (Downham et al. 1990). Figures 10c and 17b illustrates that OH3-coated steel gain a thick oxide scale than OH1, which might be due to the higher (0.8) wt-%age of Ce in Cr<sub>3</sub>C<sub>2</sub>–NiCr coating as compared to 0.4wt% of Ce added Cr<sub>3</sub>C<sub>2</sub>–NiCr coating. Authors Zinkevich et al. (2006), and Muhich (2017) reported higher ratio of Ce may increase the oxygen vacancies concentration, resulting in more (Cr<sup>3+</sup>) cations required to cover the generated vacancies (sites) in the oxide scale as discussed in the above section. The ceria modified (OH5) Cr<sub>3</sub>C<sub>2</sub>–NiCr coating with 1.2wt-% of CeO<sub>2</sub> revealed a higher weight gain (3.363 mg/cm<sup>2</sup>) than its counterparts. Higher weight gain might be due to a higher concentration of ceria in the conventional coating. During the initial oxidation cycles, the colour of the OH5-coated sample transformed from light grey to dark grey with green patches, which could be attributed to the initiation of the oxide scale (Liu et al. 2019). Minor black spots were also seen on the surface of the coating, which may be attributed to the oxidation reaction. The main phases revealed by XRD analysis (Fig. 8e) are Cr<sub>2</sub>O<sub>3</sub>, Cr<sub>3</sub>C<sub>2</sub>, NiCr<sub>2</sub>O<sub>4</sub>, CeO<sub>2</sub>, and CeCrO<sub>3</sub>. The chemical reactions responsible for the development of these oxides are given in Eqs. 3, 5, 6, 9, and 10, respectively. Figure 15 (X-ray map) revealed that the oxide layer of chromium is mainly responsible for the protection of bare steel along with spinels of nickel and cerium. The phases revealed by XRD analysis were reported to be protective under corrosive environments (Shao et al. 2012; Mudgal et al. 2014). However, spallation of oxides in the form of tiny particles was observed on the surface of the coating. Coating spallation in the form of tiny particles might be due to the high ratio (1.2wt-%) of Ce in carbide coating. Various authors reported that rare earth is beneficial if they were added to coating in small fractions (Naumenko et al. 2016; Vishnoi et al. 2020). Various researchers (Cambon et al. 2012; Shao et al. 2012; Rehman et al. 2021) reported that a high ratio (wt.%) of rare earth elements promotes oxygen vacancies concentration and nucleation sites for the oxide scale but also promotes porosity/cavities inside the oxide scale might be due to difference between oxygen vacancies and chromia nucleation sites.

Figure 17 represents the oxide layer structure for ceria-added Cr<sub>3</sub>C<sub>2</sub>–NiCr coatings (OH, OH1, OH3, and OH5) after 50 cycles of oxidation. The gap that arises between vacancies and nucleation sites may reduce oxide scale adhesion, as observed in the OH5-coated steel (Fig. 17d). Various Authors (Yi et al. 2000; Chęćmanowski et al. 2013; Cai et al. 2018; Wang et al. 2019) have reported that a higher ratio of the rare earth in surface deposited coatings may reduce the adhesion and microhardness as well as reduce oxidation resistance. A lower value of microhardness is also observed for OH5 coating doped with a higher amount

of Ce than OH1- and OH3-coated steels, as depicted in Fig. 2. Pang et al. (2016a) reported that a higher concentration of cerium increases the microporosity of the coating or oxide scale; simultaneously, the oxidation resistance of coated substrate decreases. Oxidation morphology results of the ceria-modified coated steel illustrate that the addition of CeO<sub>2</sub> in coating hinders the growth of oxide scale and assists the Cr-rich oxide layer, which enhances the oxidation resistance of chromium carbide coatings (Cueff et al. 2004; Pang et al. 2016a). From the weight change analysis Fig. 6 and SEM/EDS analysis (Fig. 10b–d), it is observed that the cerium element speed up the initial oxidation to build up a protective layer early than undoped Cr<sub>3</sub>C<sub>2</sub>-NiCr coating, resulting in a thin oxide scale. A mechanism has been proposed for conventional and Cr<sub>2</sub>C<sub>3</sub>-NiCr coating modified with different fractions of ceria after subjecting oxidizing environment at 750 °C for 50 cycles and has been shown in Fig. 18.

## 5 Conclusions

1. Microhardness of the conventional and ceria modified coatings was measured as OH coating-854Hv, OH1 coating-925Hv, OH3 coating-966Hv, and OH5 coating-895Hv. Ceria element improves the microhardness of the Cr<sub>3</sub>C<sub>2</sub>-NiCr coating if added in optimum wt-%age. Moreover, the microporosity of the coating was also enhanced with a minimum concentration of Ce. Similarly, the surface roughness of the coating decreased with increasing the concentration of cerium.
2. Bare steel TP347H possesses higher weight gain due to oxidation, but no spallation of oxide scale was evidenced during the cyclic study, which might be due to the presence of chromium (71.53 wt.%) and nickel (11.42 wt.%) in austenite steel. The main phases revealed in oxidized TP347H steel are Fe<sub>2</sub>O<sub>3</sub> along with NiFe<sub>2</sub>O<sub>4</sub> and NiCr<sub>2</sub>O<sub>4</sub> spinels.
3. Cr<sub>3</sub>C<sub>2</sub>-NiCr-coated TP347H steel showed good oxidation resistance with minor crack and spallation of oxide scale. Oxides of Cr<sub>2</sub>O<sub>3</sub> with NiCr<sub>2</sub>O<sub>4</sub> spinels are mainly responsible for increasing the oxidation resistance. The main reason behind the crack and spallation of oxide scale is thermal stress developed during thermal fluctuation during cycles study at 750 °C. The repetitions of heating and cooling reduce the oxide scale plasticity.
4. Cr<sub>3</sub>C<sub>2</sub>-NiCr coating modified with different contents (0.4wt-%, 0.8wt-%, and 1.2wt-%) of CeO<sub>2</sub> provided better protection in the oxidizing atmosphere, possibly due to the existence of Cr<sub>2</sub>O<sub>3</sub>, Cr<sub>3</sub>C<sub>2</sub>, NiCr<sub>2</sub>O<sub>4</sub>, and Cr<sub>23</sub>C<sub>6</sub>. The auxiliary phases in ceria-modified coatings are Ce<sub>2</sub>O<sub>3</sub> and CeCrO<sub>3</sub>, primarily responsible for enhancing the oxidation resistance of Cr<sub>3</sub>C<sub>2</sub>-NiCr coating after creating hindrance to metal cation (Cr, Ni). The variation in the thickness of various samples is as follows: OH1-coated steel-20 μm, OH3-coated steel-35 μm, OH5-coated steel-45 μm, OH-coated steel-50 μm. Moreover, thin (lower thickness than OH sample) and a compact oxide layer formed after the addition of Ce, enhancing the oxide scale's plasticity
5. Cr<sub>3</sub>C<sub>2</sub>-NiCr coating (OH1) doped with 0.4wt-% of CeO<sub>2</sub> exhibited better oxidation resistance followed by OH3, and OH5, doped with 0.8wt-% and 1.2 wt-% of CeO<sub>2</sub>, respectively. However, a higher concentration of Ce in Cr<sub>3</sub>C<sub>2</sub>-NiCr coating loosens the adhesion of the oxide scale.
6. NiCr<sub>2</sub>O<sub>4</sub> spinels and Cr<sub>23</sub>C<sub>6</sub>, Cr<sub>7</sub>C<sub>3</sub> phases have enhanced the oxidation resistance of coated TP347H steel samples.

## Declarations

**Conflict of interest** The authors declare no conflict of interest.

## References

- Ahuja L, Mudgal D (2019) High temperature corrosion performance of ceria doped Cr<sub>3</sub>C<sub>2</sub>-NiCr coated superalloys under actual medical waste atmosphere. *Mater Today Proc* 28:599–603. <https://doi.org/10.1016/j.matpr.2019.12.228>
- Babu S, Thanneeru R, Inerbaev T, Day R, Masunov AE, Schulte A, Seal S (2009) Dopant-mediated oxygen vacancy tuning in ceria nanoparticles. *Nanotechnology*. <https://doi.org/10.1088/0957-4484/20/8/085713>
- Botu V, Ramprasad R, Mhadeshwar AB (2014) Ceria in an oxygen environment: Surface phase equilibria and its descriptors. *Surf Sci* 619:49–58. <https://doi.org/10.1016/j.susc.2013.09.019>
- Cai G, Li C (2015) Effects of Ce on inclusions, microstructure, mechanical properties, and corrosion behavior of AISI 202 stainless steel. *J Mater Eng Perform* 24:3989–4009. <https://doi.org/10.1007/s11665-015-1651-6>
- Cai Y, Luo Z, Chen Y (2018) Effect of CeO<sub>2</sub> on TiC morphology in Ni-based composite coating. *High Temp Mater Process* 37:209–217. <https://doi.org/10.1515/htmp-2016-0198>
- Cambon JB, Esteban J, Ansart F, Bonino JP, Turq V, Santagneli SH, Santilli CV, Pulcinelli SH (2012) Effect of cerium on structure modifications of a hybrid sol-gel coating, its mechanical properties and anti-corrosion behavior. *Mater Res Bull* 47:3170–3176. <https://doi.org/10.1016/j.materresbull.2012.08.034>
- Chatha SS, Sidhu HS, Sidhu BS (2012) High temperature hot corrosion behaviour of NiCr and Cr<sub>3</sub>C<sub>2</sub>-NiCr coatings on T91 boiler steel in an aggressive environment at 750°C. *Surf Coatings Technol* 206:3839–3850. <https://doi.org/10.1016/j.surfcoat.2012.01.060>
- Chawla V, Chawla A, Puri D, Prakash S, Gurbuxani PG, Sidhu BS (2011) Hot corrosion & erosion problems in coal based power plants in India and possible solutions—a review. *J Miner Mater Charact Eng* 10:367–386. <https://doi.org/10.4236/jmmce.2011.104027>
- Chęćmanowski J, Matraszek A, Szczygieł I, Szczygieł B (2013) High-temperature oxidation of FeCrAl alloy with alumina-silica-ceria



- coatings deposited by sol–gel method. *J Therm Anal Calorim* 113:311–318. <https://doi.org/10.1007/s10973-013-3014-6>
- Chen SF, Liu SY, Wang Y, Sun XG, Zou ZW, Li XW, Wang CH (2014) Microstructure and properties of HVOF-sprayed NiCrAlY coatings modified by rare earth. *J Therm Spray Technol* 23:809–817. <https://doi.org/10.1007/s11666-014-0097-y>
- Chen Z, Li S, Wu M, Pei Y, Gong S, Zhang H (2020a) Effects of different surface native pre-oxides on the hot corrosion properties of nickel-based single crystal superalloys. *Materials (basel)* 13:5774. <https://doi.org/10.3390/ma13245774>
- Chen Z, Qin M, Yang J, Zhang L, Jia B, Qu X (2020b) Effect of  $\text{La}_2\text{O}_3$  addition on the synthesis of tungsten nanopowder via combustion-based method. *J Mater Sci Technol* 58:24–33. <https://doi.org/10.1016/j.jmst.2020.03.069>
- Choudhury B, Chetri P, Choudhury A (2015) Annealing temperature and oxygen-vacancy-dependent variation of lattice strain, band gap and luminescence properties of  $\text{CeO}_2$  nanoparticles. *J Exp Nanosci* 10:103–114. <https://doi.org/10.1080/17458080.2013.801566>
- Col A, Parry V, Pascal C (2017) Oxidation of a Fe–18Cr–8Ni austenitic stainless steel at 850 °C in  $\text{O}_2$ : Microstructure evolution during breakaway oxidation. *Corros Sci* 114:17–27. <https://doi.org/10.1016/j.corsci.2016.10.029>
- Colson JC, Buscail H, Bonnet G, Lachkar M, Larpin JP (1995) The effect of deposited rare earth oxide films on high temperature corrosion behaviour of different metals and alloys. *Solid State Phenom* 41:165–176. <https://doi.org/10.4028/www.scientific.net/SSP.41.165>
- Cueff R, Buscail H, Caudron E, Riffard F, Issartel C, El Messki S (2004) Effect of reactive element oxide coating on the high temperature oxidation behaviour of FeCrAl alloys. *Appl Surf Sci* 229:233–241. <https://doi.org/10.1016/j.apsusc.2004.01.072>
- Da Cunha CA, Correa OV, Sayeg IJ, Ramanathan LV (2017) High temperature erosion-oxidation resistance of thermally sprayed nanostructured  $\text{Cr}_3\text{C}_2$ -25(Ni-20Cr) coatings. *Mater Res* 20:994–1002. <https://doi.org/10.1590/1980-5373-MR-2015-0611>
- Ding Y, Hussain T, McCartney DG (2015) High-temperature oxidation of HVOF thermally sprayed NiCr– $\text{Cr}_3\text{C}_2$  coatings: microstructure and kinetics. *J Mater Sci* 50:6808–6821. <https://doi.org/10.1007/s10853-015-9238-z>
- Downham DA, Hussey RJ, Mitchell DF, Graham MJ (1990) Segregation of cerium in chromia scales. In: High-Temperature oxid sulphidation process, pp 101–112. <https://doi.org/10.1016/B978-0-08-040423-3.50013-6>
- Esposito V, Ni DW, He Z, Zhang W, Prasad AS, Glasscock JA, Chatzichristodoulou C, Ramousse S, Kaiser A (2013) Enhanced mass diffusion phenomena in highly defective doped ceria. *Acta Mater* 61:6290–6300. <https://doi.org/10.1016/j.actamat.2013.07.012>
- Fan C, Shi J, Sharafiev A, Lemmens P, Dilger K (2020) Optical spectroscopic and electrochemical characterization of oxide films on a ferritic stainless steel. *Mater Corros* 71:440–450. <https://doi.org/10.1002/maco.201911425>
- Gada H, Mudgal D, Parvez S, Ahmad B (2020) Investigation of high temperature corrosion resistance of Ni25Cr coated and bare 347H SS in actual husk fired boiler atmosphere. *Eng Fail Anal* 108:104256. <https://doi.org/10.1016/j.engfailanal.2019.104256>
- Ghadami F, Zakeri A, Aghdam ASR, Tahmasebi R (2019) Structural characteristics and high-temperature oxidation behavior of HVOF sprayed nano- $\text{CeO}_2$  reinforced NiCoCrAlY nanocomposite coatings. *Surf Coatings Technol* 373:7–16. <https://doi.org/10.1016/j.surfcoat.2019.05.062>
- Ghadami F, Sabour Rouh Aghdam A, Ghadami S (2021) A comprehensive study on the microstructure evolution and oxidation resistance of conventional and nanocrystalline MCrAlY coatings. *Sci Rep* 11:875. <https://doi.org/10.1038/s41598-020-79323-w>
- Gheno T, Monceau D, Young DJ (2012) Mechanism of breakaway oxidation of Fe–Cr and Fe–Cr–Ni alloys in dry and wet carbon dioxide. *Corros Sci* 64:222–233. <https://doi.org/10.1016/j.corsci.2012.07.024>
- Ghosh D, Mitra SK (2011) High temperature corrosion problem of boiler components in presence of sulfur and alkali based fuels. *High Temp Mater Process* 30:81–85. <https://doi.org/10.1515/hmp.2011.011>
- Goyal R, Singh K, Chawla V, Sidhu BS, Singh K (2012) High temperature oxidation and carbon nano tubes—an overview. *High Temp* 5762:55–58
- Goyal A, Singh R, Singh G (2017) Study of high-temperature corrosion behavior of D-Gun spray coatings on ASTM-SA213, T-11 steel in molten salt environment. *Mater Today Proc* 4:142–151. <https://doi.org/10.1016/j.matpr.2017.01.007>
- Guo W, Wu Y, Zhang J, Hong S, Chen L, Qin Y (2015) A comparative study of cyclic oxidation and sulfates-induced hot corrosion behavior of arc-sprayed Ni–Cr–Ti coatings at moderate temperatures. *J Therm Spray Technol* 24:789–797. <https://doi.org/10.1007/s11666-015-0222-6>
- Habib KA, Damra MS, Saura JJ, Cervera I, Bellés J (2011) Breakdown and evolution of the protective oxide scales of AISI 304 and AISI 316 stainless steels under high-temperature oxidation. *Int J Corros*. <https://doi.org/10.1155/2011/824676>
- Han ZK, Zhang L, Liu M, Ganduglia-Pirovano MV, Gao Y (2019) The structure of oxygen vacancies in the near-surface of reduced  $\text{CeO}_2$  (111) under strain. *Front Chem* 7:1–12. <https://doi.org/10.3389/fchem.2019.00436>
- Houdková Š, Černý J, Pala Z, Haušild P (2015) High temperature resistance of selected HVOF coatings. *Key Eng Mater* 662:111–114. <https://doi.org/10.4028/www.scientific.net/KEM.662.111>
- Houdková Š, Česánek Z, Smazalová E, Lukáč F (2018) The high-temperature wear and oxidation behavior of CrC-based HVOF coatings. *J Therm Spray Technol* 27:179–195. <https://doi.org/10.1007/s11666-017-0637-3>
- Huang X, Xiao K, Fang X, Xiong Z, Wei L, Zhu P, Li X (2020) Oxidation behavior of 316L austenitic stainless steel in high temperature air with long-term exposure. *Mater Res Express* 7:66517. <https://doi.org/10.1088/2053-1591/ab96fa>
- Huiming J, Linnan Z, Xiaojun L (2007) Influence of nanometric  $\text{CeO}_2$  coating on high temperature oxidation of Cr. *Oxid Met* 17:601–606
- Kadgaye C, Hasan SM, Patra S, Ghosh M, Nath SK, Karmakar A (2021) Role of cerium on transformation kinetics and mechanical properties of low carbon steels. *Metall Mater Trans A Phys Metall Mater Sci* 52:3978–3995. <https://doi.org/10.1007/s11661-021-06358-7>
- Kamal S, Sharma KV (2016) Study of oxidation behavior of thermal spray coating on superalloys at 900 °C. *Appl Mech Mater* 819:553–562. <https://doi.org/10.4028/www.scientific.net/AMM.819.553>
- Kamal S, Jayaganthan R, Prakash S (2011) Hot corrosion studies of detonation-gun-sprayed NiCrAlY + 0.4 wt.%  $\text{CeO}_2$  coated superalloys in molten salt environment. *J Mater Eng Perform* 20:1068–1077. <https://doi.org/10.1007/s11665-010-9728-8>
- Kaur M, Singh H, Prakash S (2009) High-temperature corrosion studies of HVOF-sprayed Cr 3C 2-NiCr coating on SAE-347h boiler steel. *J Therm Spray Technol* 18:619–632. <https://doi.org/10.1007/s11666-009-9371-9>
- Kawamura K, Nakashima T, Maruyama T (1998) Effect of superficial application of yttrium oxides with various activities on high temperature oxidation of chromium. *Mater Trans JIM* 39:747–755. <https://doi.org/10.2320/matertrans1989.39.747>
- Khanna AS (2016) Fundamentals of high temperature oxidation/corrosion. In: High temperature corrosion. World Scientific Book. [https://doi.org/10.1142/9789814675239\\_0001](https://doi.org/10.1142/9789814675239_0001)
- Kitamura K, Nishiyama Y, Fujimoto S, Otsuka N (2019) Stress and adhesion of protective oxide scales on stainless steels

- and Re effects. *ISIJ Int* 59:1642–1649. <https://doi.org/10.2355/isijinternational.ISIJINT-2019-037>
- Ksiazek M, Boron L, Radecka M, Richert M, Tchorz A (2016) Mechanical and tribological properties of HVOF-sprayed ( $\text{Cr}_3\text{C}_2\text{-NiCr+Ni}$ ) composite coating on ductile cast iron. *J Mater Eng Perform* 25:3185–3193. <https://doi.org/10.1007/s11665-016-2226-x>
- Kumar S, Mudgal D, Singh S, Prakash S (2014) Effect of  $\text{CeO}_2$  in  $\text{Cr}_3\text{C}_2\text{-NiCr}$  coating on superni 600 at high temperature. *Proc Mater Sci* 6:939–949. <https://doi.org/10.1016/j.mspro.2014.07.164>
- Kumar S, Kumar M, Handa A (2018) Combating hot corrosion of boiler tubes—a study. *Eng Fail Anal* 94:379–395. <https://doi.org/10.1016/j.engfailanal.2018.08.004>
- Kumar M, Mudgal D, Ahuja L (2019a) Evaluation of high temperature oxidation performance of bare and coated T91 steel. *Mater Today Proc* 28:620–624. <https://doi.org/10.1016/j.matpr.2019.12.232>
- Kumar S, Kumar M, Handa A (2019b) Comparative study of high temperature oxidation behavior and mechanical properties of wire arc sprayed Ni–Cr and Ni–Al coatings. *Eng Fail Anal* 106:104173. <https://doi.org/10.1016/j.engfailanal.2019.104173>
- Li H, Chen W (2010) Stability of  $\text{MnCr}_2\text{O}_4$  spinel and  $\text{Cr}_2\text{O}_3$  in high temperature carbonaceous environments with varied oxygen partial pressures. *Corros Sci* 52:2481–2488. <https://doi.org/10.1016/j.corsci.2010.02.040>
- Li H, Cui X, Chen W (2010) Effect of  $\text{CeO}$  on high temperature carburization behavior of Mn–Cr–O spinel and chromium oxide. *J Electrochem Soc* 157:C321. <https://doi.org/10.1149/1.3478659>
- Li X, Shu J, Chen L, Bi H (2014) Effect of cerium on high-temperature oxidation resistance of  $00\text{Cr}17\text{NbTi}$  ferritic stainless steel. *Acta Metall Sin Eng Lett* 27:501–507. <https://doi.org/10.1007/s40195-014-0079-6>
- Liang B, Zhang Z, Guo H (2016) Tribological behavior of thermal spray and fusing ni-based alloy coatings with rare earth cerium under reciprocating sliding. *Trans Indian Inst Met* 69:1943–1950. <https://doi.org/10.1007/s12666-015-0764-9>
- Liu S, Wu X, Weng D, Ran R (2015) Ceria-based catalysts for soot oxidation: a review. *J Rare Earths* 33:567–590. [https://doi.org/10.1016/S1002-0721\(14\)60457-9](https://doi.org/10.1016/S1002-0721(14)60457-9)
- Liu Q, Bai Y, Wang HD, Ma GZ, Liu M, Chu CY, Sun YW, Fan W, Ding F, Zhao B, Wang YT (2019) Microstructural evolution of carbides and its effect on tribological properties of SAPS or HVOF sprayed NiCr– $\text{Cr}_3\text{C}_2$  coatings. *J Alloy Compd* 803:730–741. <https://doi.org/10.1016/j.jallcom.2019.06.291>
- Liu E, Wang F, Du S, Zeng Z, Du H, Bai Y (2020a) Effect of  $\text{Cr}_2\text{O}_3$  on the microstructure and tribological performance of sprayed Fe-based coating on cylinder liner. *Proc Inst Mech Eng Part J J Eng Tribol* 234:435–447. <https://doi.org/10.1177/1350650119870964>
- Liu H, Huang Y, Wang X, Lu R (2020b) Effect of  $\text{CeO}_2$  on high-temperature oxidation performance of electron beam cladding NiCoCrAlY coating on Ni-based alloy. *Adv Mater Sci Eng* 2020:1–6. <https://doi.org/10.1155/2020/8731315>
- Lone SA, Eatoo MA, Rahman A (2019) Degradation behaviour of nanostructured  $\text{CeO}_2$  films on superalloy. *Trans Indian Inst Met* 72:793–800. <https://doi.org/10.1007/s12666-018-1532-4>
- Mahesh RA, Jayaganthan R, Prakash S (2010) A study on the oxidation behavior of HVOF sprayed NiCrAlY-0.4 wt.%  $\text{CeO}_2$  coatings on superalloys at elevated temperature. *Mater Chem Phys* 119:449–457. <https://doi.org/10.1016/j.matchemphys.2009.09.024>
- Mathapati M, Doddamani M, Ramesh MR (2018) High-temperature erosive behavior of plasma sprayed  $\text{Cr}_3\text{C}_2\text{-NiCr}$ /cenosphere coating. *J Mater Eng Perform* 27:1592–1600. <https://doi.org/10.1007/s11665-018-3226-9>
- Matthews S, Berger L-M (2019) Inter-diffusion between thermally sprayed  $\text{Cr}_3\text{C}_2\text{-NiCr}$  coatings and an Alloy 625 substrate during long-term exposure at 500°C, 700°C and 900°C. *J Alloys Compd* 770:1078–1099. <https://doi.org/10.1016/j.jallcom.2018.08.189>
- Mehta J, Mittal VK, Gupta P (2017) Role of thermal spray coatings on wear, erosion and corrosion behavior: A review. *J Appl Sci Eng* 20:445–452. <https://doi.org/10.6180/jase.2017.20.4.05>
- Mittal A, Albertsson GJ, Gupta GS, Seetharaman S, Subramanian S (2014) Some thermodynamic aspects of the oxides of chromium. *Metall Mater Trans B Process Metall Mater Process Sci* 45:338–344. <https://doi.org/10.1007/s11663-014-0027-x>
- Mudgal D, Kumar S, Singh S, Prakash S (2014) Corrosion behavior of bare,  $\text{Cr}_3\text{C}_2\text{-25%NiCr}$ , and  $\text{Cr}_3\text{C}_2\text{-25%NiCr+0.4%CeO}_2$ -coated superni 600 under molten salt at 900 °C. *J Mater Eng Perform* 23:3805–3818. <https://doi.org/10.1007/s11665-014-1177-3>
- Mudgal D, Singh S, Prakash S (2015) Evaluation of ceria-added  $\text{Cr}_3\text{C}_2\text{-25NiCr}$  coating on three superalloys under simulated incinerator environment. *J Therm Spray Technol* 24:496–514. <https://doi.org/10.1007/s11666-014-0209-8>
- Muhich CL (2017) Re-evaluating  $\text{CeO}_2$  expansion upon reduction: noncounterpoised forces, not ionic radius effects, are the cause. *J Phys Chem C* 121:8052–8059. <https://doi.org/10.1021/acs.jpcc.6b12373>
- Muthu SM, Venkateshkannan M, Gupta S, Surya Prakash K, Arivarasu M, Arivazhagan N (2020) Investigation of Air oxidation and hot corrosion behavior of Boiler grade material Austenitic stainless steel AISI 347. *Mater Today Proc* 22:1694–1701. <https://doi.org/10.1016/j.matpr.2020.02.187>
- Naumenko D, Pint BA, Quadackers WJ (2016) Current thoughts on reactive element effects in alumina-forming systems. In memory of John Stringer. *Oxid Met* 86:1–43. <https://doi.org/10.1007/s11085-016-9625-0>
- Nijdam TJ, Sloof WG (2007) Effect of reactive element oxide inclusions on the growth kinetics of protective oxide scales. *Acta Mater* 55:5980–5987. <https://doi.org/10.1016/j.actamat.2007.07.007>
- Nithin HS, Nishchitha KM, Shamanth V, Hemanth K, Babu KA (2020) High-temperature oxidation and corrosion behaviour of APS CoCrAlY +  $\text{Cr}_3\text{C}_2\text{-NiCr}$  composite coating. *J Bio-Tribo-Corrosion* 6:1–11. <https://doi.org/10.1007/s40735-020-0322-9>
- Nyadongo ST, Pityana SL, Olakanmi EO (2021) Isothermal oxidation performance of laser cladding assisted with preheat (Lcap) triballoy t-800 composite coatings deposited on en8. *Coatings*. <https://doi.org/10.3390/coatings11070843>
- Pang Q, Hu ZL, Sun DL (2016a) The influence of Ce content and preparation temperature on the microstructure and oxidation behavior of Ce-modified Cr coating on open-cell Ni–Cr–Fe alloy foam. *Vacuum* 129:86–98. <https://doi.org/10.1016/j.vacuum.2016.04.018>
- Pang Q, Hu ZL, Wu GH (2016b) Preparation and oxidation performance of Y and Ce-modified Cr coating on open-cell Ni–Cr–Fe alloy foam by the pack cementation. *J Mater Eng Perform* 25:5189–5200. <https://doi.org/10.1007/s11665-016-2362-3>
- Panicaud B, Grosseau-Poussard JL, Dinhut JF (2006) On the growth strain origin and stress evolution prediction during oxidation of metals. *Appl Surf Sci* 252:5700–5713. <https://doi.org/10.1016/j.apsusc.2005.07.075>
- Patil S, Seal S, Guo Y, Schulte A, Norwood J (2006) Role of trivalent la and Nd dopants in lattice distortion and oxygen vacancy generation in cerium oxide nanoparticles. *Appl Phys Lett* 88:2004–2007. <https://doi.org/10.1063/1.2210795>
- Perez N (2016) *Electrochemistry and corrosion science*, 2nd edn. Springer, Cham. <https://doi.org/10.1007/978-3-319-24847-9>
- Pillis MF, de Araújo EG, Ramanathan LV (2006) Effect of addition of rare earth oxide concentrates on oxidation resistance of AISI 304L. *Mater Sci Forum* 530–531:99–104. <https://doi.org/10.4028/www.scientific.net/MSF.530-531.99>
- Prabhakaran D, Jegadeeswaran, (2021) Oxidation resistance by HVOF coating on gas turbine Superco-605 material. *Mater Today Proc* 45:54–57. <https://doi.org/10.1016/j.matpr.2020.09.236>

- Purkayastha S, Dwivedi DK (2014) Abrasive and erosive wear performance of rare earth oxide doped Ni/WC coatings. *J Tribol* 136:1–9. <https://doi.org/10.1115/1.4025099>
- Qu Y, Xing J, Zhi X, Peng J, Fu H (2008) Effect of cerium on the as-cast microstructure of a hypereutectic high chromium cast iron. *Mater Lett* 62:3024–3027. <https://doi.org/10.1016/j.matlet.2008.01.129>
- Rahman A, Jayaganthan R (2016) Study of nanostructured CeO<sub>2</sub> coatings on superalloy. *Surf Eng* 32:771–778. <https://doi.org/10.1080/02670844.2016.1148381>
- Rehman K, Sheng N, Sang Z, Xun S, Wang Z, Xie J, Hou G, Zhou Y, Sun X (2021) Comparative study of the reactive elements effects on oxidation behavior of a Ni-based superalloy. *Vacuum* 191:110382. <https://doi.org/10.1016/j.vacuum.2021.110382>
- Saladi S, Menghani J, Prakash S (2015) Effect of CeO<sub>2</sub> on cyclic hot-corrosion behavior of detonation-gun sprayed Cr<sub>3</sub>C<sub>2</sub>-NiCr coatings on Ni-based superalloy. *J Mater Eng Perform* 24:1379–1389. <https://doi.org/10.1007/s11665-015-1400-x>
- Saroop V, Mudgal D, Kumar S, Prakash S (2020) Evaluation of corrosion mechanism for tungsten carbide coating exposed in actual boiler environment. *Eng Fail Anal* 118:104905. <https://doi.org/10.1016/j.engfailanal.2020.104905>
- Schmucker E, Petitjean C, Martinelli L, Panteix PJ, Ben Lagha S, Vilasi M (2016) Oxidation of Ni-Cr alloy at intermediate oxygen pressures. I. Diffusion mechanisms through the oxide layer. *Corros Sci* 111:474–485. <https://doi.org/10.1016/j.corsci.2016.05.025>
- Shao M, Cui L, Zheng Y, Xing L (2012) Effect of cerium addition on oxidation behavior of 25Cr20Ni alloy under low oxygen partial pressure. *J Rare Earths* 30:164–169. [https://doi.org/10.1016/S1002-0721\(12\)60016-7](https://doi.org/10.1016/S1002-0721(12)60016-7)
- Sharma S (2012) Erosive wear study of rare earth-modified hvo-f-sprayed coatings using design of experiment. *J Therm Spray Technol* 21:49–62. <https://doi.org/10.1007/s11666-011-9688-z>
- Sharma SP, Dwivedi DK, Jain PK (2008) Effect of CeO<sub>2</sub> addition on the microstructure, hardness, and abrasive wear behaviour of flame-sprayed Ni-based coatings. *Proc Inst Mech Eng Part J J Eng Tribol* 222:925–933. <https://doi.org/10.1243/13506501JET432>
- Shi Z, Shi D, Gao B, Xu J, Hu X, Wang Z (2012) Oxidation of Fe-Ni Alloys in Air at 700°C, 800°C and 950°C. *High Temp Mater Process* 31:89–96. <https://doi.org/10.1515/htmp.2011.147>
- Shi M, Xue Z, Liang H, Yan Z, Liu X, Zhang S (2020) High velocity oxygen fuel sprayed Cr<sub>3</sub>C<sub>2</sub>-NiCr coatings against Na<sub>2</sub>SO<sub>4</sub> hot corrosion at different temperatures. *Ceram Int* 46:23629–23635. <https://doi.org/10.1016/j.ceramint.2020.06.135>
- Shu D, Cui X, Li Z, Sun J, Wang J, Chen X, Dai S, Si W (2020) Effect of the rare earth oxide CeO<sub>2</sub> on the microstructure and properties of the Nano-WC-reinforced Ni-based composite coating. *Metals (basel)* 10:1–16. <https://doi.org/10.3390/met10030383>
- Shukla R, Bera AK, Yusuf SM, Deshpande SK, Tyagi AK, Hermes W, Eul M, Pöttgen R (2009) Multifunctional nanocrystalline CeCrO<sub>3</sub>: antiferromagnetic, relaxor, and optical properties. *J Phys Chem C* 113:12663–12668. <https://doi.org/10.1021/jp903013u>
- Shukla VN, Jayaganthan R, Tewari VK (2015) Degradation behavior of HVOF-sprayed Cr<sub>3</sub>C<sub>2</sub>-25%NiCr cermet coatings exposed to high temperature environment. *Mater Today Proc* 2:1805–1813. <https://doi.org/10.1016/j.matpr.2015.07.048>
- Singh K, Goyal K, Goyal R (2019) Hot corrosion behaviour of different Cr<sub>3</sub>C<sub>2</sub>-NiCr coatings on boiler tube steel at elevated temperature. *World J Eng* 16:452–459. <https://doi.org/10.1108/WJE-02-2019-0049>
- Siripongsakul T, Thublaor T, Prajakesakul V, Kachaban S, Chandra-Ambhorn S (2017) Chromia evaporation of ferritic stainless steel AISI430 coated by (La, Sr)CrO<sub>3</sub> perovskite and Mn-Co spinel. *Key Eng Mater* 728:166–171. <https://doi.org/10.4028/www.scientific.net/KEM.728.166>
- Song X, Wang L, Liu Y, Ma H (2011) Effects of temperature and rare earth content on oxidation resistance of Ni-based superalloy. *Prog Nat Sci Mater Int* 21:227–235. [https://doi.org/10.1016/S1002-0071\(12\)60035-5](https://doi.org/10.1016/S1002-0071(12)60035-5)
- Sreenivasulu V, Manikandan M (2018) Hot corrosion studies of HVOF sprayed carbide and metallic powder coatings on alloy 80A at 900 °C. *Mater Res Express* 6:036519. <https://doi.org/10.1088/2053-1591/aaf65d>
- Stefan E, Neagu D, Blennow Tullmar P, Persson ÅH, Sudireddy BR, Miller D, Chen M, Irvine J (2017) Spinel-based coatings for metal supported solid oxide fuel cells. *Mater Res Bull* 89:232–244. <https://doi.org/10.1016/j.materresbull.2017.02.003>
- Thakare JG, Pandey C, Mulik RS, Mahapatra MM (2019) Microstructure and mechanical properties of D-Gun sprayed Cr<sub>3</sub>C<sub>2</sub>-NiCr coating on P91 steel subjected to long term thermal exposure at 650 °C. *Mater Res Express*. <https://doi.org/10.1088/2053-1591/ab5265>
- Thanneeru R, Patil S, Deshpande S, Seal S (2007) Effect of trivalent rare earth dopants in nanocrystalline ceria coatings for high-temperature oxidation resistance. *Acta Mater* 55:3457–3466. <https://doi.org/10.1016/j.actamat.2007.01.043>
- Veselkov S, Samoiloova O, Shaburova N, Trofimov E (2021) High-temperature oxidation of high-entropic alloys: a review. *Materials* 14(10):2595. <https://doi.org/10.3390/ma14102595>
- Vishnoi M, Murtaza Q, Kumar P (2020) Materials today : proceedings effect of rare earth elements on coatings developed by thermal spraying processes ( TSP )—a brief review. *Mater Today Proc*. <https://doi.org/10.1016/j.matpr.2020.10.439>
- Wang X, Szpunar JA (2017) Effect of CeO<sub>2</sub> coating on the isothermal oxidation behaviour of Ni-based alloy 230. *Oxid Met* 88:565–582. <https://doi.org/10.1007/s11085-016-9692-2>
- Wang Q, Yao Q, Song JZ, Wang Y, Zhu YH, Lu T, Han BJ (2017) Effect of rare earth element on the oxidation behavior of novel γ/γ'-strengthened Co-9Al-10W alloys. *J Mater Res* 32:2117–2126. <https://doi.org/10.1557/jmr.2017.14>
- Wang W, Chen Z, Feng S (2019) Effect of CeO<sub>2</sub> on impact toughness and corrosion resistance of WC reinforced Al-based coating by laser cladding. *Materials (basel)* 12:1–15. <https://doi.org/10.3390/ma12182901>
- Wang J, Zhou G, He R, Huang W, Zhu J, Mao C, Wu C, Lu G (2020) Experimental preparation and optical properties of CeO<sub>2</sub>/TiO<sub>2</sub> heterostructure. *J Mater Res Technol* 9:9920–9928. <https://doi.org/10.1016/j.jmrt.2020.06.053>
- Wei W, Xu C, Zhang J, Cheng W, Niu X (2014) Effects of Ce addition on microstructure, mechanical properties and corrosion resistance of as-cast AZ80 magnesium alloy. *China Foundry* 11:157–162
- Wu YC, Lin CC (2014) The microstructures and property analysis of aliovalent cations (Sm<sup>3+</sup>, Mg<sup>2+</sup>, Ca<sup>2+</sup>, Sr<sup>2+</sup>, Ba<sup>2+</sup>) co-doped ceria-base electrolytes after an aging treatment. *Int J Hydrogen Energy* 39:7988–8001. <https://doi.org/10.1016/j.ijhydene.2014.03.063>
- Wu S, Guo B, Li T, Gui D (2015) Oxidation of chromium carbide coated Q235 steel in wet and dry air at 750 °C. *Constr Build Mater* 81:11–14. <https://doi.org/10.1016/j.conbuildmat.2015.01.072>
- Wu Y, Yan Q, Zhang X (2020) Wear characteristics of Fe-based diamond composites with cerium oxide (CeO<sub>2</sub>) reinforcements. *Int J Refract Met Hard Mater* 86:105093. <https://doi.org/10.1016/j.ijrmhm.2019.105093>
- Yedong H, Wei G (2013) Theoretical consideration on composite oxide scales and coatings. *J Rare Earths* 31:435–440. [https://doi.org/10.1016/S1002-0721\(12\)60300-7](https://doi.org/10.1016/S1002-0721(12)60300-7)
- Yi W, Zheng C, Fan P, Cheng S, Li W, Ying G (2000) Effect of rare earth on oxidation resistance of iron base fluxing alloy spray-welding coating. *J Alloys Compd* 311:65–68. [https://doi.org/10.1016/S0925-8388\(00\)00863-X](https://doi.org/10.1016/S0925-8388(00)00863-X)
- Yin B, Liu G, Zhou H, Chen J, Yan F (2010) Sliding wear behavior of HVOF-sprayed Cr<sub>3</sub>C<sub>2</sub>-NiCr/CeO<sub>2</sub> composite coatings at elevated



- temperature up to 800 °C. *Tribol Lett* 37:463–475. <https://doi.org/10.1007/s11249-009-9540-5>
- You PF, Zhang X, Zhang HL, Liu HJ, Zeng CL (2018) Effect of CeO<sub>2</sub> on oxidation and electrical behaviors of ferritic stainless steel interconnects with Ni Fe coatings. *Int J Hydrogen Energy* 43:7492–7500. <https://doi.org/10.1016/j.ijhydene.2018.02.178>
- Yu XX, Taylor MA, Perepezko JH, Marks LD (2020) Competition between thermodynamics, kinetics and growth mode in the early-stage oxidation of an equimolar CoCrFeNi alloy. *Acta Mater* 196:651–659. <https://doi.org/10.1016/j.actamat.2020.06.056>
- Yu L, Zhang Y, Fu T, Wang J, Cui K, Shen F (2021) Rare earth elements enhanced the oxidation resistance of mo-si-based alloys for high temperature application: a review. *Coatings*. <https://doi.org/10.3390/coatings11091144>
- Zand RZ, Verbeken K, Adriaens A (2013) Influence of the cerium concentration on the corrosion performance of ce-doped silica hybrid coatings on hot dip galvanized steel substrates. *Int J Electrochem Sci* 8:548–563
- Zhang Z, Lu X, Luo J (2007) Tribological properties of rare earth oxide added Cr<sub>3</sub>C<sub>2</sub>–NiCr coatings. *Appl Surf Sci* 253:4377–4385. <https://doi.org/10.1016/j.apsusc.2006.09.040>
- Zhang Z, Liang B, Guo H (2014) The Effect of CeO<sub>2</sub> addition on the microstructure and properties of ni-based flame-spray coatings. *J Therm Spray Technol* 23:725–731. <https://doi.org/10.1007/s11666-014-0060-y>
- Zhang X, Liu H, Chen T, Wang G, Li H, Hu H, Yu Y, Yao H (2020) Application of coatings to alleviate fireside corrosion on heat transfer tubes during the combustion of low-grade solid fuels: a review. *Energy Fuels* 34:11752–11770. <https://doi.org/10.1021/acs.energyfuels.0c02145>
- Zhou CH, Liu AL, Ma HT, Wang L (2016) The Oxide-scale growth and failure on an Fe–16Cr alloy in the presence of compressive stress. *Oxid Met* 85:537–546. <https://doi.org/10.1007/s11085-016-9611-6>
- Zhu L, Peng X, Yan J, Wang F (2004) Oxidation of a novel chromium coating with CeO<sub>2</sub> dispersions. *Oxid Met* 62:411–426. <https://doi.org/10.1007/s11085-004-0921-8>
- Zinkevich M, Djurovic D, Aldinger F (2006) Thermodynamic modelling of the cerium-oxygen system. *Solid State Ionics* 177:989–1001. <https://doi.org/10.1016/j.ssi.2006.02.044>

**Publisher's Note** Springer Nature remains neutral with regard to jurisdictional claims in published maps and institutional affiliations.